


Fracture mechanical properties of shale and macro-meso-micro multi-scale fracture surface characteristics

Zhuo Dong^a, Xiaoyan Zhai^a, Yingxian Lang^a, Bin Gong^{b,*} , Ruifu Yuan^a, Zhuli Ren^a

^a School of Energy Science and Engineering, Henan Polytechnic University, Jiaozuo 454000, China

^b Department of Civil and Environmental Engineering, Brunel University of London, London UB8 3PH, UK

ARTICLE INFO

Keywords:

Bedding angles
Mechanical response
Failure patterns
Notched semi-circular bend
Multi-scale surface morphology

ABSTRACT

The presence of bedding planes imparts pronounced anisotropy to the mechanical behavior of shale, fundamentally influencing its response to external stress. This anisotropic behavior is critical in determining the fracturing characteristics and overall mechanical performance of shale in engineering applications, particularly in resource extraction and stability evaluations. In this study, fracture tests were conducted on shale specimens with varying bedding angles (0°, 30°, 60°, and 90°) using the notched semi-circular bend (NSCB) method. The influence of the bedding angle on fracture toughness and failure pattern was systematically investigated. Additionally, multi-scale fracture surface morphology characteristics were analyzed through 3D optical scanning, ultra-depth field microscopy, and scanning electron microscope (SEM), enabling a comprehensive evaluation of the structural effects of bedding angles. The results indicate that fracture toughness decreases with increasing bedding angle, crack propagation becomes more stable, and the dispersion of fracture toughness diminishes. The failure pattern observed can be categorized as follows: tensile failure across the bedding plane (0°), shear failure along the bedding plane with mixed failure across the bedding plane (30°), shear failure along the bedding plane or tensile failure across the bedding plane (60°), and tensile failure along the bedding plane with mixed failure across the bedding plane (90°). These distinct failure patterns underscore the critical influence of bedding angle on fracture mechanisms. Moreover, the multi-scale failure characteristics exhibit significant correlation and consistency. The fractal dimension and joint roughness coefficient (JRC) initially increase and decrease with increasing bedding angle. Based on parameters such as asperity height, slope angle, and aspect direction, quantitative morphology characterization confirms that 30° specimens exhibit the highest surface complexity. A strong correlation is observed between the fractal dimension and the standard deviation of morphology descriptors, indicating robust geometric consistency across scales. These findings provide compelling evidence for the intrinsic link between macroscopic mechanical response and microscopic fracture surface morphology, offering critical insights into the multi-scale evolution of shale failure mechanisms and furnishing a theoretical foundation for designing and optimizing fracturing strategies in anisotropic shale formations.

1. Introduction

Shale is a fine-grained sedimentary rock widely distributed in unconventional oil and gas reservoirs, distinguished by its well-developed layered structure, and pronounced anisotropic mechanical behavior. As shale resource exploitation advances, understanding its fracture behavior has become increasingly vital for achieving efficient hydraulic fracturing. The formation of organic-rich bedding planes during sedimentary diagenesis results in significant directional variability in shale's mechanical properties [1,2], exerting a strong influence on the

initiation, propagation path, and fracture surface morphology [3][4][5]. Given these anisotropic characteristics, studying shale fracture mechanics is essential for elucidating the underlying mechanisms of fracture development and establishing a theoretical framework to optimize fracturing parameters and design efficient reservoir stimulation strategies [6][7][8]. Such research is instrumental in improving the reliability and productivity of shale gas and oil extraction, contributing to the advancement of unconventional hydrocarbon recovery technologies.

Research on the influence of bedding angles on the mechanical

* Corresponding author.

E-mail address: bin.gong@brunel.ac.uk (B. Gong).

<https://doi.org/10.1016/j.tafmec.2025.105179>

Received 6 June 2025; Received in revised form 11 August 2025; Accepted 15 August 2025

Available online 18 August 2025

0167-8442/© 2025 The Authors. Published by Elsevier Ltd. This is an open access article under the CC BY license (<http://creativecommons.org/licenses/by/4.0/>).

properties of shale has predominantly focused on basic mechanical parameters such as compressive strength, tensile strength, and shear strength [9–11]. However, Mode I fracture represents a primary failure mode commonly encountered in underground engineering applications, including hydraulic fracturing and borehole stability [12,13]. Lei et al. [14] conducted experimental and numerical studies to investigate the effects of bedding properties on the fracture behaviors of shale under Mode I loading conditions. Chang et al. [15] studied the influence of cyclic thermal shock and high-temperature acid etching on the Mode I fracture properties of shale. Similarly, Vishal et al. [16] conducted a systematic investigation into the effects of thermal treatment on the fracture toughness and tensile strength of shale, aiming to enhance understanding of its deformation behavior under elevated temperature conditions. Additionally, the anisotropy of fracture toughness under dynamic loading has been increasingly reported. For example, the co-effects of bedding planes and loading conditions on Mode I fracture toughness of anisotropic rocks (shale and coal) were investigated by Shi et al. [17]. Yan et al. [18] comprehensively investigated the dynamic fracture behavior of shale under impact loading, focusing on both Mode I and Mode II fractures. These studies indicate that current research has concentrated on the fracture toughness of isotropic shale under different environmental and loading conditions (quasi-static and dynamic). However, shale's fracture toughness is not only dependent on its mineral composition and pore structure but also significantly by the orientation and configuration of bedding planes. As inherent planes of weakness, bedding planes modulate the local stress field at the crack tip and alter the energy release rate during crack propagation, resulting in pronounced anisotropic fracture behavior [19,20]. Therefore, a systematic investigation into the influence of bedding angle on the fracture mechanics of shale is crucial for advancing fracture prediction accuracy.

Due to the widespread development of bedding planes, joints, micro-cracks, and mineral fabric within the shale, crack propagation can involve complex phenomena such as bifurcation, deflection, interlayer slip, and discontinuous growth during expansion [12,18]. These processes directly influence the connectivity of the fracture network, the stimulated reservoir volume, and the formation of fracture-induced fluid flow pathways, thus profoundly affecting the efficiency of hydraulic fracturing in unconventional oil and gas reservoirs. Liu et al. [21] used numerical simulations to investigate fracture propagation paths in shale containing multiple cemented veins and bedding planes. Heng et al. [22] conducted Brazilian, direct shear, and three-point bending tests to evaluate the influence of bedding angles on failure patterns, revealing significant anisotropy in tensile strength, shear strength, and failure mechanisms. Xiao et al. [23] investigated the deep shale's fracture mechanics and crack initiation and proposed a classification of four typical initiation modes. Moreover, the fracture initiation angles and failure modes of notched semi-circular bend (NSCB) and Brazilian disc (BD) specimens in layered shales were discussed [20]. Notably, fracture development in shale exhibits distinct multi-scale characteristics. It spans from nanoscale inter-mineral microfractures and pores, mesoscale bedding parallel and interlayer fractures, and macroscale fracture networks and fault structures. This hierarchical structure exerts a significant influence on the evolution of fracture systems. While the controlling role of bedding planes is well-recognized [12,14,20,23], comprehensive research from a multi-scale perspective remains limited. Most current studies are conducted under single-scale conditions, making it difficult to fully capture the evolutionary mechanisms of fracture development across scales, thereby constraining the deeper understanding of the structural control exerted by bedding planes.

The fracture surface morphology of rock materials under different loading conditions has garnered broad research interest [15,24–26]. The fracture surface serves as a morphological “fingerprint” of the fracture process, preserving critical information regarding crack propagation paths, fracture mechanisms, and energy dissipation characteristics. For instance, Zhou et al. [27] investigated the thermal–mechanical degradation of granite under coupled loading, finding that elevated

temperatures promote gouge formation and reduce the roughness of the slip surface. Zhang et al. [28] utilized fractal dimension and morphological parameters to analyze the effect of confining pressure on the shear fracture behavior and surface morphology of granite by the short core in a compression test. Similarly, studies on sandstone subjected to cyclic freeze–thaw treatments have utilized fractal dimension, asperity height, slope angle, aspect direction, and joint roughness coefficient (JRC) to characterize fracture surface morphology [29]. Meng et al. [30] explored the role of bedding planes in the mixed-mode fracture behavior of rock-like material, particularly emphasizing the evolution of asperity height and JRC. Additionally, Ji et al. [31] analyzed the micromorphology of BD shale specimens using fracture mechanics and fractal theory. Wu et al. [32] evaluated the impacts of bedding angle on fracture characteristics and fractal dimension in NSCB shale specimens, while Zheng et al. [13] investigated how different testing methods influence the fractal dimension of fracture surfaces in Longmaxi shale under Mode-I loading.

Most studies have focused on isotropic rocks such as granite and sandstone. Shale displays markedly different crack evolution patterns due to its inherent anisotropy, weak plane development, and complex mechanical behavior. Although some studies have applied fractal dimension as a quantitative index to characterize fracture morphology [12,31,32], systematic studies on the fracture surface of shale, especially under tensile loading, remain scarce. Furthermore, investigations incorporating the multi-scale effects of bedding angle, crack path variability, and microstructure interference are still insufficient. Therefore, there is a pressing need to conduct systematic and multi-scale research on the fracture surface morphology characteristics of shale using high-precision experimental techniques.

With the above considerations, the present study performs three-point bending tests on shale specimens with different bedding angles (0°, 30°, 60°, and 90°). The key innovation of this study lies in the systematic investigation of the bedding angle's influence on mode-I fracture toughness and multiscale crack propagation characteristics, which remain underexplored in previous studies. Additionally, ultra-depth-of-field microscopic, three-dimensional optical scanning, and scanning electron microscope (SEM) are employed to examine the fracture surface. Fractal theory and statistical analysis are employed to systematically characterize the multiscale morphology evolution of fracture surfaces under varying bedding angles. The results offer new insights into the multi-scale failure mechanism of shale, contributing to a more comprehensive understanding of its fracture behavior and informing the design and stability assessment of shale gas exploitation and other geoenvironmental applications.

2. Materials and test procedure

2.1. Specimen preparation

Due to its favorable reservoir characteristics and high gas content, the Longmaxi shale is one of China's most economically viable gas resources. Obtaining intact shale specimens is challenging, as relatively intact shale cores are prone to cracking along bedding planes when unloading during drilling. The test specimens used in this study were collected from an outcrop of the Longmaxi Formation in Chongqing Province, China. The lithology is relatively straightforward, primarily consisting of fine-grained shale with distinct bedding, which is prone to cracking from weathering. The shale specimen surface was scanned using ultra-depth field microscopy, revealing obvious layered sedimentary structures ($\times 100$), as indicated by the red arrows in Fig. 1. These bedding planes are the main cause of the significant anisotropic action on the mechanics and failure behavior of shale.

Additionally, during the sampling process, the weathered surface layer of the outcrop was eliminated to obtain shale from the lower section, which exhibited superior preservation conditions, limited natural fracturing, and minimal structural disturbance. To maintain the

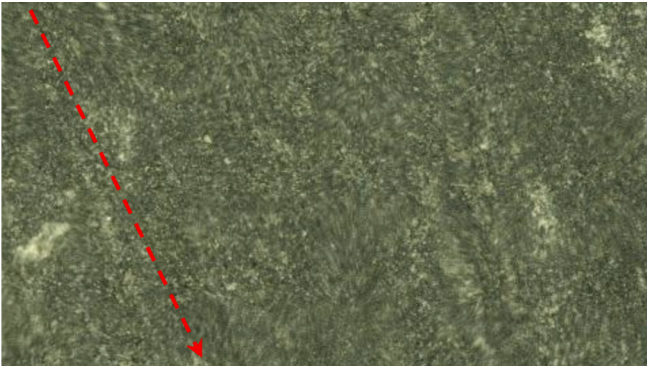


Fig. 1. Ultra-depth field microscopy image of the shale specimen surface ($\times 100$).

integrity of the physical and mechanical characteristics during transit and storage, the collected specimens were hermetically sealed to mitigate potential degradation caused by mechanical shock, moisture fluctuations, and further weathering effects.

Shale exhibits remarkable anisotropy in strength, deformation, and failure mechanisms. This study focuses primarily on the effects of bedding angles on the fracture mechanical properties of shale. Therefore, four bedding angles were considered: 0° , 30° , 60° , and 90° , as shown in Fig. 2(a). Diamond cutting wires are capable of precisely cutting shale specimens, the extent of specimen loss is minimized, and the flatness of the specimen's cut surface is maintained at a high level. These wires can also accurately create a notch in rock specimens with minimal vertical deviation. To a significant degree, they enable precise guidance of crack tip propagation in the intended direction, thereby reducing the likelihood of deviation during crack propagation and enhancing the success rate of experiments. To avoid the discreteness of test results, at least four specimens should be tested for each group, and the typical Notched semi-circular bend (NSCB) specimens are shown in Fig. 2(b).

To ensure the accuracy and comparability of test results, sample processing precision was maintained within ± 0.5 mm, with end-face parallelism within ± 0.02 mm. According to the recommendations of the International Society for Rock Mechanics (ISRM), as shown in Fig. 2

(c), the value of diameter ($2R$) was more significant than 10 times the average mineral size [33]. The thickness (B) value was sure to be $0.8R$. The pre-notch depth (a) value was ensured to satisfy $0.4 \leq a/R \leq 0.6$, and the supporting span (S) value should satisfy $0.5 \leq S/2R \leq 0.8$ [33]. Hence, the diameter and thickness of NSCB specimens are 50 mm and 25 mm, respectively. The pre-notch depth and supporting span are 10 mm and 35 mm, respectively. The prefabricated notches had a 0.4 mm width. The average geometric parameters for different bedding angles are listed in Table 1.

2.2. Experimental system and experimental procedure

The entire test system was divided into two parts: the loading system and a post-processing system, as shown in Fig. 3. The specific test system and procedure are as follows:

(1) Loading system: The study utilized the RMT-150-B rock mechanics test system at Henan Polytechnic University. This advanced system includes a support structure, hydraulic loading pump station, standard indenter, static sensor, and auxiliary system components to ensure precise control during testing. Key technical specifications include a maximum axial loading capacity of 1000 kN and a maximum axial displacement of 50 mm. Additionally, the system's deformation and stress measurement accuracy is maintained within $\pm 1.0\%$, and the device exhibits a high stiffness level, exceeding 5.0×10^9 N/mm, to minimize deformation under load. An axial LVDT measures axial displacement accurately and promptly relays data to the computer-controlled system for real-time analysis. Fig. 3 shows the NSCB specimens placed on the two supporting rollers on the loading platform. The specimens were then loaded to failure using axial displacement control with an unchanged loading rate of 0.002 mm/s. The lower loading rate

Table 1

The geometry specifications for the NSCB shale specimen.

Bedding angles / $^\circ$	D /mm	B /mm	S /mm	a /mm
0	49.94	25.34	35.0	9.99
30	49.95	25.43		10.06
60	49.93	24.99		9.94
90	49.91	25.14		9.87

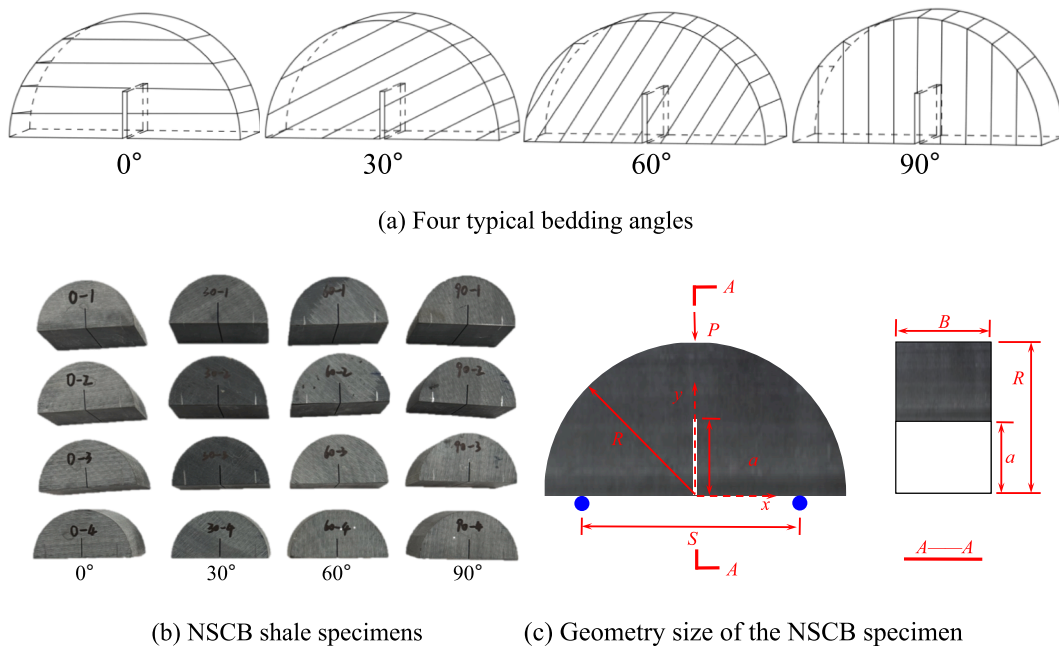


Fig. 2. Notched semi-circular bend (NSCB) shale specimens.

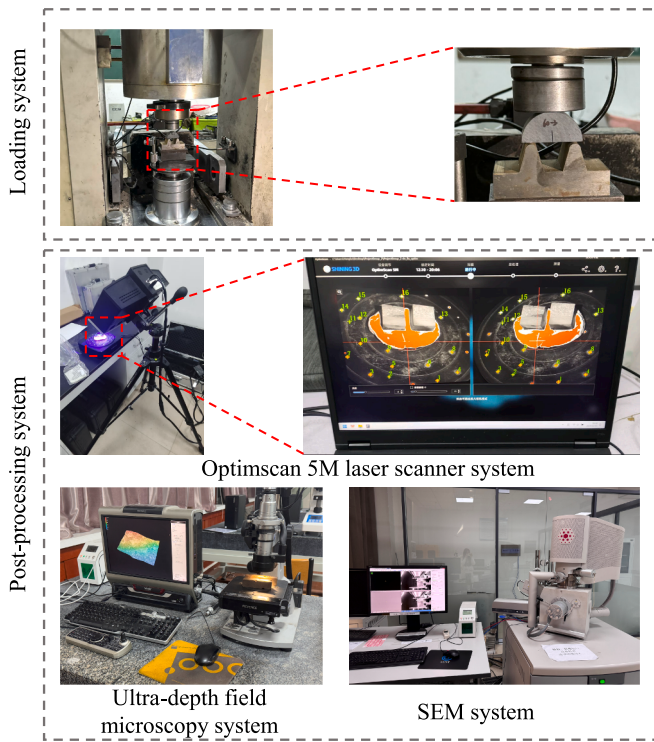


Fig. 3. Experimental system.

satisfies the requirement for static crack propagation, enabling the nonlinear fracture process zone to develop fully while avoiding dynamic fracture effects, thereby achieving more precise fracture toughness measurements.

(2) Post-processing system: This system mainly includes the Crack

3D optical scanning system (OptimScan 5 M), ultra-depth field microscopy system (VHX-2000), and scanning electron microscope (SEM) (Quanta FEG 250), as shown in Fig. 3. Crack 3D optical scanning system is used to monitor the shale fracture surface after the test, which is characterized by a measurement range of $200 \times 100 \text{ mm}^2$, average precision of 0.01 mm, average point distance of 0.08 mm, and sensor pixel of $5,000,000 \times 2$. The ultra-depth-of-field microscopy system's high-resolution image sensor enables up to 1,000x magnification with a 54-megapixel resolution, precisely capturing specimen details down to the micron scale. A Quanta 250 FEG equipped with field emission gun (FEG) capability, offering a resolution of $\sim 1.0 \text{ nm}$, was utilized for sample characterization. Before the examination, specimens were sectioned, dehydrated, and affixed to stubs using a conductive adhesive, followed by gold sputter-coating to enhance conductivity. Imaging was conducted in both secondary electron (SE) and backscattered electron (BSE) modes, complemented by energy-dispersive X-ray spectroscopy (EDS) for compositional analysis. This approach enabled the identification of microstructural features and fracture patterns on the shale fracture surfaces. Then, the effects of bedding angles on the fracture behavior of shale will be thoroughly analyzed using different testing scales.

3. Mechanical properties and failure patterns

3.1. Load-displacement curve

The load-displacement of the NSCB tests with different bedding angles are shown in Fig. 4. It is observed that the load-displacement curves can be categorized into two types:

(1) The load-displacement curves consist of four stages: compaction stage, linear elastic stage, yield stage, and post-peak decline stage. During the compaction stage, the contact between the specimens and the testing machine. Due to the strong heterogeneity of shale, micro-cracks form in the fragile regions under the load. As the load increased, these

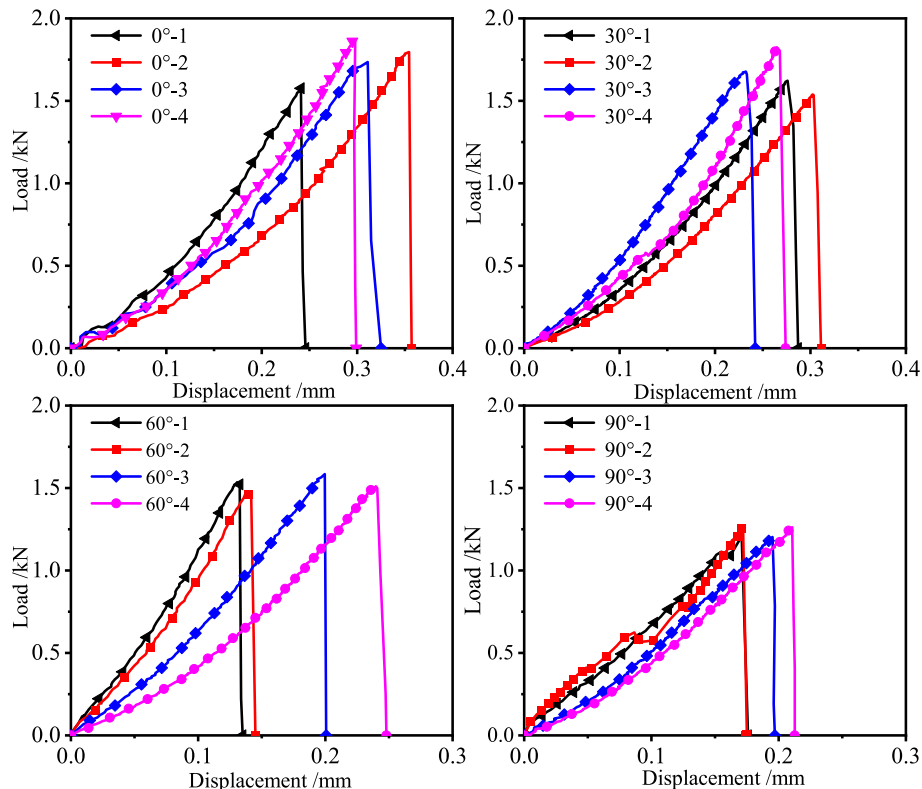


Fig. 4. Loading-displacement curves with different bedding angles.

micro-cracks gradually expanded, resulting in a typical concave-downward curve. However, it is important to note that this compaction behavior differs from that in compression tests, which is caused by micro-cracks closure. In contrast, the concave downward in the NSCB testing is caused by the initiation and expansion of new micro-cracks under tensile loading. Moreover, the load at this stage was insufficient to produce visible macroscopic cracks. In the linear elastic stage, the slope of the curve remains constant, and strain energy accumulates continuously within the specimen, with microcracks continuing to develop. The yield stage is brief, showing a concave curve. During this stage, a large number of microcracks accumulate. As they evolve, the material stiffness drops sharply, and even minor load disturbances can trigger continuous deformation. The behavior in the post-peak decline stage differs from that in compression tests, as the specimen exhibits almost no residual strength. Following a short yield stage, it rapidly declines, indicating sudden failure. Typical examples of this curve type include the four specimens with 0° and 30°, as well as 60°-3 and 60°-4. (2) The load–displacement curves consist of three stages: linear elastic stage, yield stage, and the post-peak decline stage, with no obvious compaction stage. Representative specimens include the four specimens with 90°, 60°-1, and 60°-2.

The bedding angles not only cause pronounced anisotropy in the mechanical parameters and significantly influence its deformation and failure behavior. The differences in deformation mechanisms, especially during the compaction stage, indicate that the two curve types are closely related to the macro-meso-micro fracture characteristics of shale specimens. The reason why this phenomenon occurred will be revealed in Sections 3.3. This study will integrate multiple testing techniques to systematically investigate the effect of bedding angle on the fracture mechanics behavior of shale from a multi-scale perspective.

3.2. Mechanical parameters

Shale typically exhibits a dense bedding plane, as shown in Fig. 1 and Fig. 2(b), and these bedding planes often serve as weak regions that lead to reduce strength and have a pronounced effect on the anisotropic fracture mechanical behavior of shale. Fracture toughness is a critical parameter in rock mechanics, reflecting a material's resistance to crack propagation. The greater the fracture toughness, the higher the material's ability to resist cracking. According to the ISRM recommendations, the Mode-I fracture toughness of NSCB specimens can be calculated using the following equation [33]:

$$K_{IC} = Y \frac{P_{max} \sqrt{\pi a}}{2RB} \quad (1)$$

where K_{IC} is the Mode-I fracture toughness ($\text{MPa}\cdot\text{m}^{0.5}$), P_{max} is the peak load (N), R and B are the radius and thickness of the NSCB specimens (mm), a is the depth of the pre-notch (mm), Y is the shape parameters of the NSCB specimens, which can be calculated by Eq. (2) [33].

$$Y = -1.279 + 9.516 \frac{s}{2R} - \left(0.47 + 16.457 \frac{s}{2R}\right) \frac{a}{R} + \left(1.071 + 34.401 \frac{s}{2R}\right) \left(\frac{a}{R}\right)^2 \quad (2)$$

where S is the supporting span.

The Mode I fracture toughness of NSCB specimen with different bedding angles was calculated according to Eqs. (1) and (2), are illustrated in Table 2. It can be found that the peak load continuously decreased with the increasing bedding angle. This indicated that the bedding plane effect was strengthened with the increasing bedding angle, which is also consistent with the previous studies. Moreover, according to Eqs. (1) and (2), the variation tendency of fracture

Table 2

Fracture load under various bedding angles.

Specimens number	P_{max} /kN	Y	K_{IC} / $\text{MPa}\cdot\text{m}^{0.5}$
0°-1	1.576	1.742	4.591
0°-2	1.796		4.603
0°-3	1.736		4.602
0°-4	1.861		4.599
30°-1	1.061	1.665	4.742
30°-2	1.539		4.618
30°-3	1.677		4.543
30°-4	1.825		4.595
60°-1	1.535	1.524	4.742
60°-2	1.463		4.618
60°-3	1.585		4.543
60°-4	1.511		4.595
90°-1	1.114	1.216	4.742
90°-2	1.267		4.618
90°-3	1.203		4.563
90°-4	1.262		4.595

toughness with bedding angles is like that of peak load, and peak load is linearly related to the fracture toughness.

Fig. 5 shows the Box-whisker plots of fracture toughness. As shown in Fig. 2(a) and Fig. 5(a), the fracture toughness of shale exhibit pronounced anisotropy with various bedding angles. Specifically, when the pre-notch is perpendicular to the bedding plane (0°), the fracture toughness reaches a maximum average value of $1.1209 \text{ MPa}\cdot\text{m}^{0.5}$. As the bedding angle increases, fracture toughness gradually decreases, reaching a minimum average value of $0.7838 \text{ MPa}\cdot\text{m}^{0.5}$, where the pre-notch is parallel to the bedding plane (90°). Specifically, compared to the average fracture toughness at 0°, the average fracture toughness decreased by 4.19 %, 7.76 %, and 18.11 %, respectively. This trend highlights the dominant influence of bedding angle on crack propagation. For 90° specimens, the crack propagates along the weakest path (bedding plane), encountering minimal resistance, thereby reducing the overall fracture toughness. These results indicate that bedding planes serve as either “crack-guiding” or “crack-blocking” structures, depending on their orientation, and play a critical role in controlling fracture toughness.

From the perspective of micro-fracture mechanisms and energy evolution, shale comprises brittle minerals such as quartz and feldspar, interspersed with poorly cemented clay minerals, forming a distinct layered structure, as shown in Fig. 1. For 0° specimens, cracks must traverse the mineral matrix arranged perpendicular to the bedding planes, resulting in transgranular microcracks. This process involves energy dissipation through interfacial cracking, mineral grain breakage, crack deflection, and branching, leading to a tortuous fracture path and higher energy consumption. In contrast, for 90° specimens, cracks predominantly follow the mechanically weaker bedding planes, where crack propagation is primarily interfacial. Here, energy is mostly consumed by interfacial separation and frictional sliding, resulting in lower fracture energy dissipation and, consequently, the lowest fracture

toughness. This shift from “matrix-controlled” to “interface-controlled” energy dissipation underlies the observed reduction in fracture toughness.

Fig. 5 (b) illustrates a statistical analysis of fracture toughness under different bedding angles. The results indicate that higher standard deviations and coefficients of variation at 0° and 30° (approximately 0.075 and 0.065, respectively), indicating significant variability in fracture toughness. As the bedding angle increases to 60° and 90°, the standard

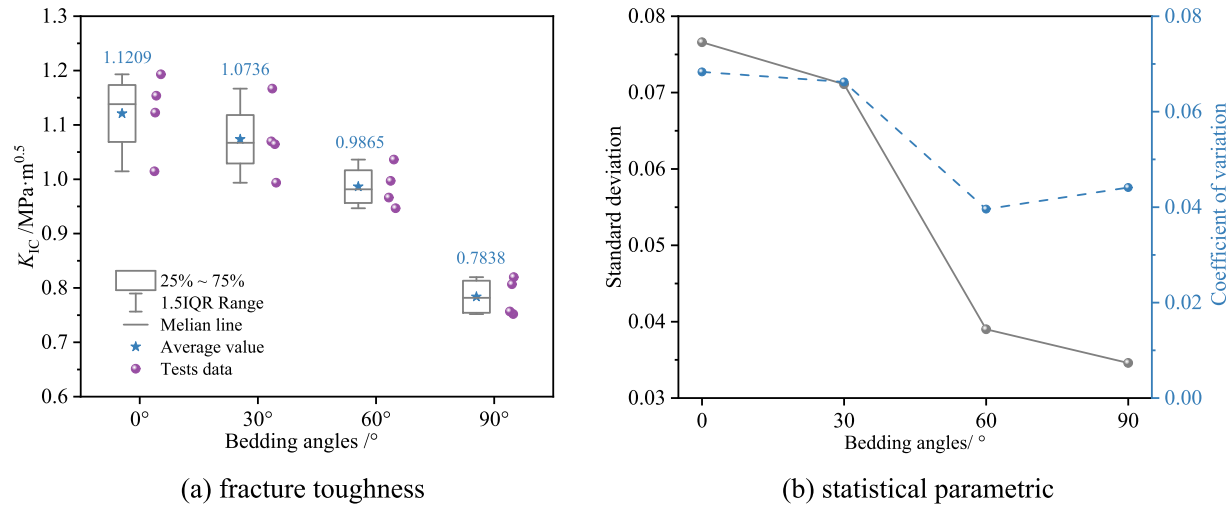


Fig. 5. Fracture toughness under different bedding angles.

deviation drops below 0.035, and the coefficient of variation stabilizes near 0.04. This trend is further supported by the box plots in Fig. 5 (a), which reveal the widest distribution and the highest number of outliers at 0°, indicating pronounced structural randomness and variability in stress response. This variability arises from the need for cracks to penetrate the heterogeneous shale matrix at low bedding angles, making the crack propagation path highly sensitive to microstructural features such as mineral grain size, pore distribution, and interlayer microcracks. In contrast, at higher bedding angles (especially 90°), cracks propagate more consistently along continuous weak planes, leading to simpler failure patterns and reduced result dispersion.

The mechanical parameters indicate that the layered shale demonstrates clear fracture anisotropy across different bedding angles. The angle between the crack path and bedding planes significantly influences fracture toughness. As the bedding angle increases, the fracture mode shifts from complex transgranular cracking through the matrix to low-energy interfacial sliding and separation, resulting in reduced fracture toughness and decreased variability in test results. These findings also have important engineering implications for optimizing hydraulic fracturing strategies and selecting mechanical parameters in shale reservoirs. For reservoirs with vertical bedding plane (90°), natural weak interfaces can be exploited for low-pressure fracture initiation, allowing the main fracture to extend along the bedding plane and maximize reservoir contact. In contrast, reservoirs with horizontal bedding plane (0°) require higher injection pressures or viscosity-enhanced fracturing fluids to penetrate the matrix. In formations with intermediate bedding angles (30° or 60°), adjusting injection rates can stimulate crack deflection, promoting complex fracture network

Table 3

Failure patterns under various bedding angles.

Specimen numbers	Failure patterns
0°-1	Tensile failure across the bedding plane
0°-2	
0°-3	
0°-4	
30°-1	Shear failure along the bedding plane with mixed failure across the bedding plane
30°-2	
30°-3	
30°-4	
60°-1	Shear failure along the bedding plane
60°-2	
60°-3	
60°-4	
90°-1	Tensile failure along the bedding plane
90°-2	
90°-3	
90°-4	

formation through the competing matrix and interface energy dissipation mechanisms.

3.3. Failure patterns and failure mechanisms

The failure patterns with various bedding angles are presented in Fig. 6 and Table 3. As illustrated in Fig. 6, all cracks initiate at the pre-notch tips. Still, the crack patterns and propagation paths differ

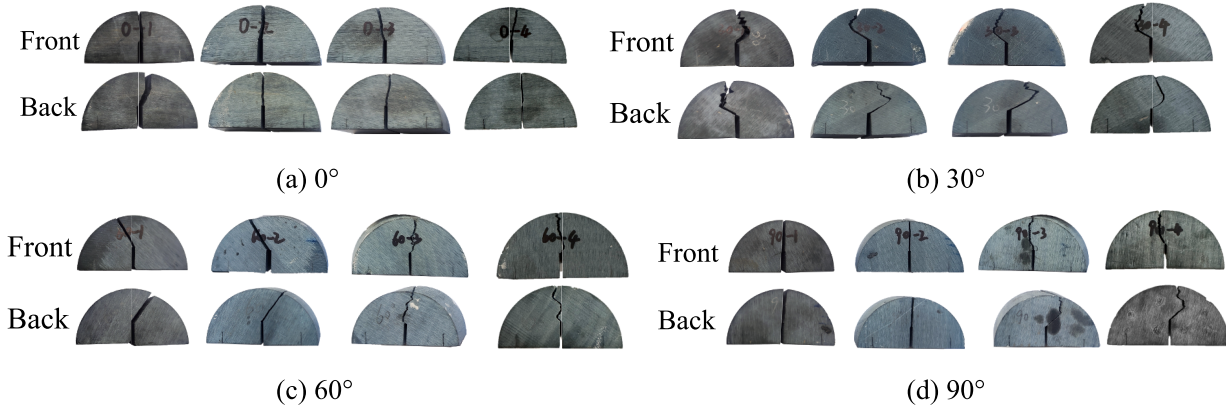


Fig. 6. Failure patterns under different bedding angles.

significantly due to the competing effects of crack deflection along the weak bedding plane and crack penetration driven by the principal stress, as detailed below.

As shown in Fig. 6(a), for both front and back side of the specimen, the crack preferentially grows in the direction perpendicular to the bedding planes under far-field tensile stress. However, due to the low cohesion and tensile strength between the bedding planes, the crack may deflect or bifurcate along these interfaces, causing slight deviation from the vertical plane of the pre-notch. Despite this, the overall crack propagation path aligns with the loading direction, that is, the direction of maximum principal stress, exhibiting typical tensile failure characteristics. Moreover, as shown in Fig. 7(a), the crack penetrates the bedding plane at 0° , requiring it to overcome frictional resistance, which increases fracture energy and reflects the anisotropic fracture behavior of layered rocks. Additionally, bedding distribution position and thickness variations influence the degree and direction of crack propagation path deflection.

As shown in Fig. 6(b) and Fig. 7(b), the crack exhibits a distinct mixed failure characteristic. The angle between the pre-notch tip stress field and the bedding plane creates competition between the direction of the maximum tensile stress and the weak bedding plane. Initially, the crack propagates along the direction of principal stress. Upon encountering the weak bedding region, a dual energy dissipation mechanism emerges: (1) shear stress induces frictional sliding, forming a shear failure along the bedding plane; (2) normal stress drives the crack to penetrate the interface, resulting in localized mixed failure characteristics. For both front and back side of specimen, experimental observations show that the crack deflects markedly along the bedding direction, then exhibits periodic “Z”-shaped turns, ultimately tending toward the loading direction. This indicates that the crack must simultaneously overcome matrix fracture toughness and interfacial friction at 30° .

When the bedding angle increases to 60° , two typical crack propagation patterns are observed, as shown in Fig. 6(c) and Table 3. 60° -1 and 60° -2 specimens exhibit shear failure along the bedding plane, as shown in Fig. 7(c). In contrast, 60° -3 and 60° -4 specimens show tensile cracks across the bedding plane, as also depicted in Fig. 7(d). These differences are primarily attributed to variations in bedding distribution position, thickness, and interfacial bond strength. For instance, when the interfacial bonding weakens, higher bedding angles are more likely to produce cracks along the bedding plane. Conversely, stronger interfacial bonding favors cross-bedding crack formation. Additionally, compared to the 0° case, cross-bedding cracks at 60° are more tortuous, with increased surface roughness.

When the bedding angle reaches 90° , the bedding direction is parallel to the pre-notch and loading direction, and crack propagation is

dominated by the weak bedding plane, as shown in Fig. 6(d). The stress field at the pre-notch tip aligns with the bedding direction, facilitating crack propagation along the weak plane with minimal resistance, occasionally jumping between adjacent layers (the front side of the specimen), as shown in Fig. 6(d) and Fig. 7(e). However, some specimens (e.g., the back side of 90° -3 and 90° -4 specimens) exhibited asymmetry and local deflections in the crack propagation path, as shown in Fig. 7(f). This suggests that even under identical bedding angles, variations in internal microstructure, local bedding bond strength, and small-scale defects can introduce slight disturbances to crack propagation. Additionally, the energy required for crack propagation is significantly reduced, and the tensile strength becomes direction-dependent. This phenomenon reveals that the weak bedding planes guide crack propagation paths, consistent with the principle that anisotropic cracks propagate along the path of least energy dissipation.

NSCB testing primarily to measure Mode I fracture toughness. Previous studies suggest that if the crack deviates less than $0.05D$ from the vertical plane of the pre-notch, the test remains valid. Significantly deviations caused by complex stress fields introduce shear components, resulting in mixed Mode I-II fracture toughness or “apparent fracture toughness”. Based on the NSCB results, fracture toughness values at 0° and 90° are considered “true fracture toughness”, while those at 30° and 60° reflect “apparent fracture toughness”. Given the complex bedding angles in unconventional reservoirs and the challenges in accurately controlling perforation during hydraulic fracturing, NSCB testing at various bedding angles is practically significant. It helps elucidate the influence of the bedding plane on shale’s fracture mechanism.

Moreover, the load–displacement curves under different bedding angles exhibit two typical characteristics: one with an initial compaction stage and one without, as shown in Fig. 4. Combined with the failure patterns in Fig. 6 and Fig. 7, it is evident that shear failures or tensile failures propagating along the bedding planes (e.g., 90° , 60° -1, and 60° -2) lack a compaction stage. This is due to the relatively low strength of bedding planes, allowing failure without microcracks accumulation. However, tensile failures propagating across the bedding planes or mixed failures (e.g., 0° , 30° , 60° -3, and 60° -4) typically exhibit a pronounced compaction stage, indicating the simultaneous damage of both bedding planes and matrix, with numerous microcracks formation. These findings reveal shale’s deformation mechanism at initial loading stages across different bedding angles, as interpreted from failure patterns.

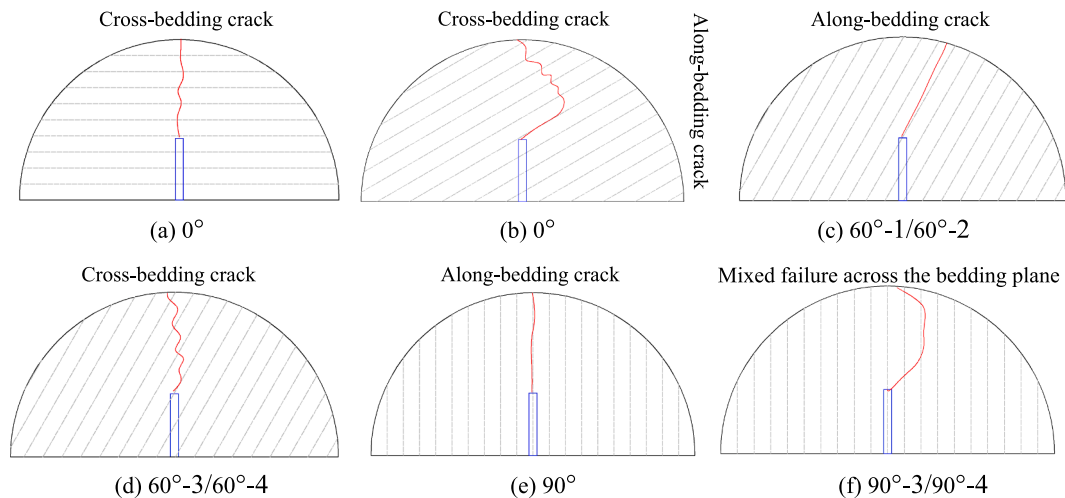


Fig. 7. Sketches of failure patterns under different bedding angles.

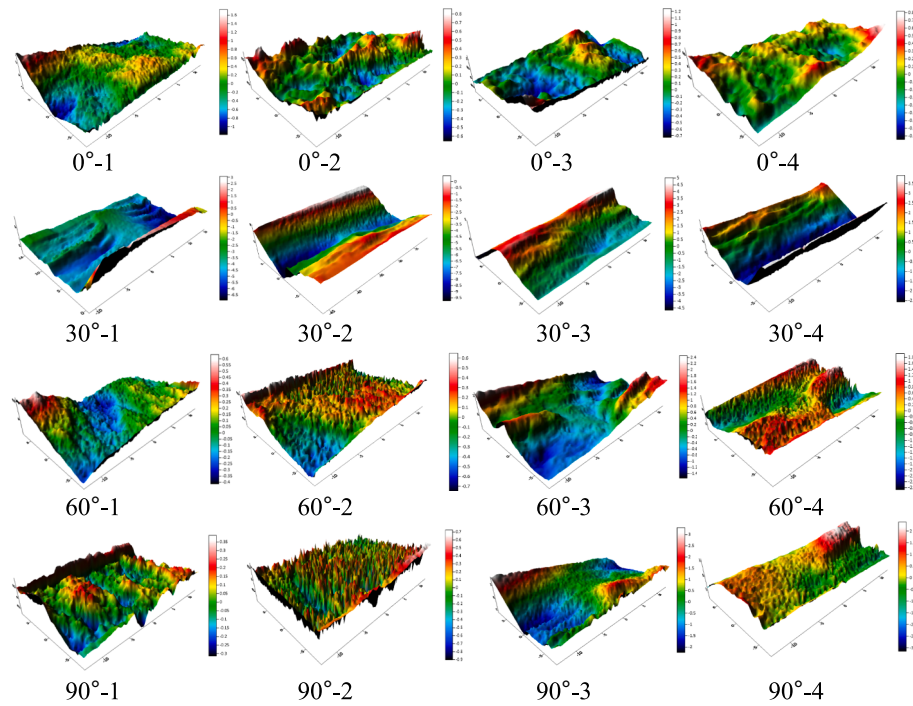


Fig. 8. Fracture surface morphology under different bedding angles.

4. Fracture surface morphology characteristics

Figs. 6 and 7 demonstrate that the bedding angles exert a significant anisotropic influence on both the crack propagation path and failure patterns. Beyond the macroscopic propagation path, a comprehensive investigation of fracture surface morphology across multiple scales (macro-meso-micro) is essential for understanding the complex fracture mechanical response of shale. At a macroscopic scale, morphology parameters such as surface height, roughness, and fractal dimension quantitatively reflect the energy released during fracture. These characteristics offer insight into the role of anisotropy in controlling fracture toughness and tensile strength, and they provide valuable guidance for predicting the effectiveness of reservoir fracturing simulation at the engineering scale. At the mesoscopic scale, attention is directed toward mineral grain arrangement, bonding conditions along bedding interfaces, and the spatial distribution of micro-crack networks. The influence of bedding angles on crack deflection, branching, and energy dissipation mechanisms can be elucidated through ultra-depth field microscopy technology, revealing the process of transition of failure patterns governed by bedding planes. Scanning electron microscopy

(SEM) is used at a microscopic scale to observe the micro-morphology of fracture surfaces and analyze crack propagation paths between mineral crystals. This enables the identification of the underlying fracture mechanisms associated with different orientations. Consequently, multi-scale coupling research supports the development of a framework linking “structural characteristics-fracture mechanism-mechanical response”. Such a model offers cross-scale scientific insight for optimizing bedding configuration and refining fracturing parameters, ultimately enhancing the efficiency of shale gas development.

4.1. Fractal dimension

The fracture surface roughness significantly influences fluid flow behavior. In this section, the fracture surfaces were scanned using a 3D optical scanning system (OptimScan 5 M). MATLAB R2023a processed the resulting data, and the 3D surface morphology maps are presented in Fig. 8. The fracture surfaces at various bedding angles exhibit different roughness characteristics. For 30° specimens, the fracture surface displays pronounced undulations and notable height differences, indicating that bedding-induced disturbances and bifurcation strongly influence crack propagation. These suggest a coupled mechanism involving bedding control and multi-surface crack interactions, contributing to a more complex interface and increased instability in the crack propagation path. This surface morphology characteristic closely correlates with the specimen's macroscopic failure mode. As shown in Figs. 6 and 7, the front part predominantly undergoes shear failure along the bedding plane, resulting in relatively smooth surfaces. However, the rear part exhibits intense mixed failure behavior, producing a distinct high-low undulating structure and increased surface roughness. For 60°-1 and 60°-2 specimens, cracks propagate primarily along the bedding plane as a shear failure, with relatively rough surfaces and height difference generally within 1.0 mm. In contrast, the 0°, 60°-3, and 60°-4 specimens display tensile cracks that cross the bedding plane, accompanied by greater height difference. The 90°-1 and 90°-2 specimens also primarily exhibit tensile failure along the bedding planes, with height differences comparable to those of 60°-1 and 60°-2. However, bedding position, thickness, and bonding strength variations result in deviations during crack propagation, leading to larger height fluctuations. Direct visual

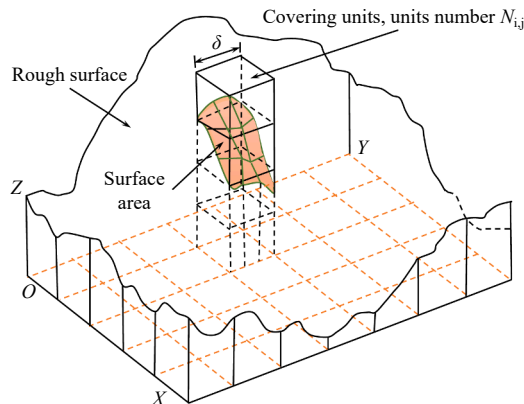


Fig. 9. Differential cubic covering methods (DCCM) schematic diagram [34].

comparison of fracture surface roughness based on 3D surface morphology images is inherently subjective and limited. Therefore, it is essential to conduct a quantitative analysis of roughness parameters to accurately evaluate surface characteristics and fracture behavior under different bedding angles.

In this study, the fractal dimension was used to analyze the fracture surface roughness. The box-counting method is a multi-scale quantification technique based on fractal theory, which is widely applied in the roughness characterization of irregular geometric bodies (such as rock fracture surfaces) [34]. Its core assumption is that the fracture surfaces exhibit statistical self-similarity, meaning that the local roughness features remain unchanged in the fractal dimension under different observation scales. By using a grid system covering the two-dimensional

where D is the fractal dimension, and previous studies indicate that the larger the fractal dimension, the rougher the fracture surface.

In the box-counting method, determining the total number of boxes $N(\delta)$ is a critical step in evaluating the fractal dimension. The differential cubic covering method (DCCM) is employed to calculate $N(\delta)$ in this study, as illustrated in Fig. 9 [34]. This method provides a very simple way to calculate the fractal dimension of a fracture surface directly. When a box with side length δ is used to cover the irregular surface projected onto a reference plane, the maximum and minimum heights within each unit cell $(i, j)_{th}$ determine the number of boxes required. This process is quantified using Eq. (4), allowing for the assessment of the three-dimensional coverage of the irregular surfaces within each region [29,34].

$$N_{ij} = INT \left[\frac{1}{\delta} \max(h_{1,1}(i, j), \dots, h_{q,k}(i, j), \dots, h_{\delta/S_0+1, \delta/S_0+1}(i, j)) \right] - INT \left[\frac{1}{\delta} \min(h_{1,1}(i, j), \dots, h_{q,k}(i, j), \dots, h_{\delta/S_0+1, \delta/S_0+1}(i, j)) \right] + 1 \quad (4)$$

or three-dimensional point cloud data of the fracture surface (obtained through laser scanning or optical profilometer), the scaling relationship between the minimum number of boxes required for coverage ($N(\delta)$) and the box size (δ) is calculated by Eq. (3) [29,34].

$$N(\delta) \propto \delta^{-D} \quad (3)$$

where INT is the rounding function, S_0 is the sampling interval. Then, the total number of boxes $N(\delta)$ needed to cover the whole fracture surface is calculated by Eq. (5) [29,34].

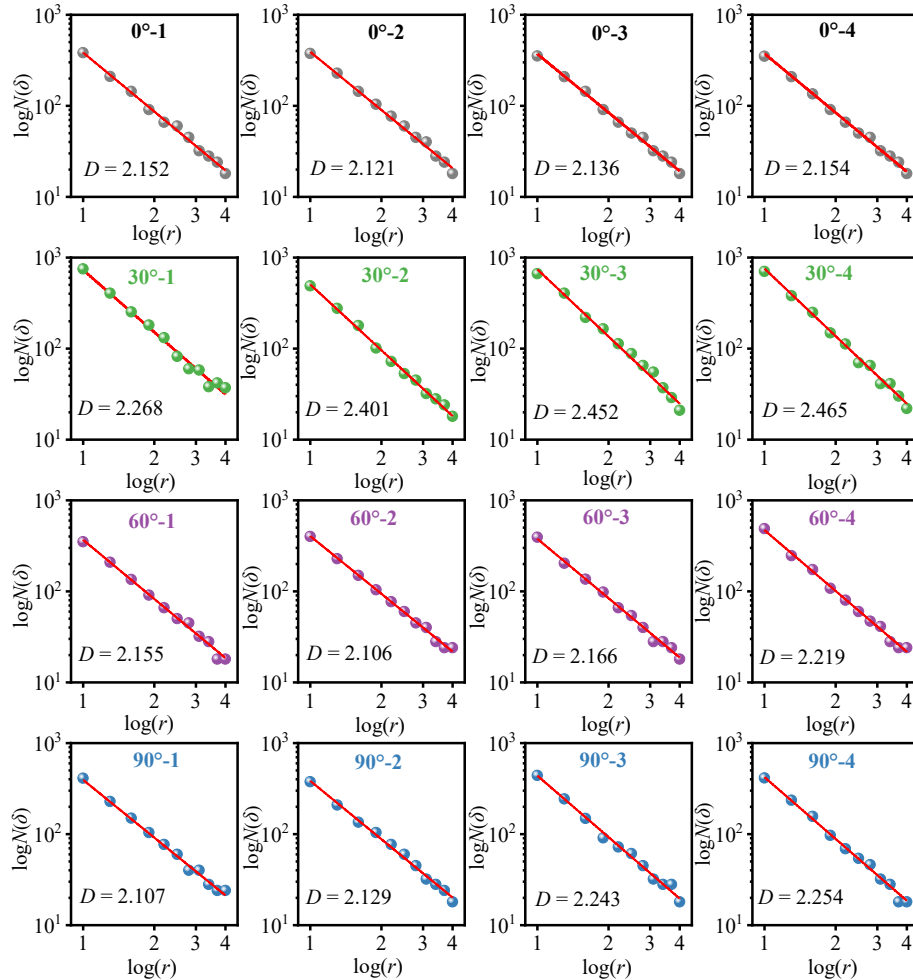


Fig. 10. Fitting results of $\log N(\delta)$ and $\log(\delta)$ with different bedding angles.

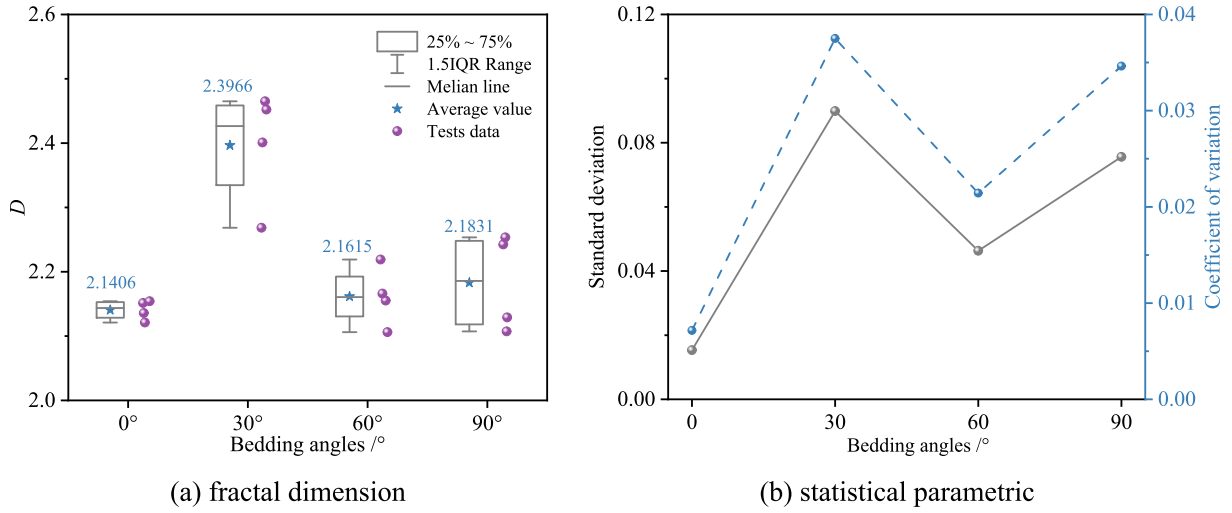


Fig. 11. Fractal dimension under different bedding angles.

$$N(\delta) = \sum_{i=1}^{(n-1)S_0/\delta} \left[\sum_{j=1}^{(m-1)S_0/\delta} N_{ij} \right] \quad (5)$$

For a specific fracture surface exhibits fractal behavior, its fractal dimension can be calculated by Eq. (3). Taking logarithmic transformation of this power law, a straight line with slope $-D$ can be obtained, which the fractal dimension can be determined, as illustrated in Eq. (6) [29]. The fitting results of $\log N(\delta)$ and $\log(\delta)$ with different bedding angles are presented in Fig. 10. The strong linearity of the fitted curves indicates that the fracture surface exhibits obvious self-similarity and fractal characteristics. Across all subplots, the data points align with the fitted lines in the double logarithmic coordinate system, demonstrating significant linear correlation. These results confirm that the fracture surface morphology can be effectively quantified using the fractal dimension. Moreover, the fractal dimension under different bedding angles range from 2.107 to 2.465, consistent with the previous studies that its values for the rough fracture surface are greater than 2.0 [28].

$$D = \frac{\log[N(\delta)]}{\log(\delta)} \quad (6)$$

The fracture surface morphology was statistically analyzed using the fractal dimension, as shown in Fig. 11(a). The results reveal a nonlinear relationship between the fractal dimension and the bedding angles. The average fractal dimensions for 0°, 60°, and 90° specimens are 2.1406, 2.1615, and 2.1831, respectively, with relatively narrow value ranges. These suggest consistent surface morphology and stable crack propagation paths. In contrast, the average fractal dimension for 30° specimens exhibits a significantly higher average fractal dimension of 2.3966, along with the largest variation range, indicating that the crack propagation path is most strongly influenced by the bedding plane. The increased complexity and multi-path propagation lead to a markedly rougher fracture surface. These confirm that cracks at 30° are more susceptible to deflection and bifurcation, forming a typical multi-scale rough surface.

To further characterize the variability in surface complexity, statistical analysis was conducted for the fractal dimensions of each specimen, including standard deviation (Std) and coefficient of variation (CV), as shown in Fig. 11(b). The 0° specimens exhibited the lowest Std and CV values, showing more stable fracture surface morphology. This stability is attributed to Mode-I tensile failure predominance across the bedding planes. The 30° specimens had the highest mean fractal dimension and the largest Std (~ 0.09) and CV (~ 0.037), reflecting significant surface morphology variability among specimens. This variability is primarily

due to the dominant mixed Mode I-II failure pattern and the increased propagation complexity in the later stages.

The 60° specimens showed intermediate Std and CV values, which were lower than the 30° but higher than 0°. These are due to the contrasting failure patterns observed: the 60°-1 and 60°-2 specimens formed Mode II shear failure along the bedding plane, resulting in smoother surfaces, while the 60°-3 and 60°-4 specimens underwent Mode I tensile failure across the bedding plane, increasing roughness and contributing to variability. For 90° specimens, the Std and CV values increased again, primarily due to heterogeneities in bedding position, thickness, and bonding strength. These factors introduced stronger anisotropy in crack propagation paths, particularly in 90°-3 and 90°-4 specimens, resulting in greater fluctuations in fracture surface morphology characteristics.

4.2. Statistical analysis of fracture surface morphology

4.2.1. Frequency distribution function

To investigate the variation patterns of fracture surface morphology under different bedding angles, this study conducted a systematic statistical analysis of key surface parameters, such as asperity height (h), slope angle (α), and aspect direction (β) [28,29]. By examining the frequency histograms of these morphology parameters, both normal and gamma distribution functions were employed to fit the observed data [35]. This approach aims to reveal the distribution trends and statistical characteristics of fracture surface geometry under different bedding angles.

(1) Normal distribution function

The probability density of the normal variable X can be expressed by Eq. (7), which obey normal distribution ($X \sim N(\mu, \sigma^2)$) [35].

$$f(x) = \frac{1}{\sqrt{2\pi}\sigma} e^{-\frac{(x-\mu)^2}{2\sigma^2}} \quad (7)$$

where $\mu = \bar{x}$ is the mean values and σ is the variance.

Some distribution patterns are not symmetrical on both sides of the normal curve, but rather lean towards one side in terms of degree and direction, or have differences in the degree of sharpness. The skewness (Sk_p) and kurtosis (K_p) can be used to measure the differences between this curve and the normal distribution curve, as expressed by Eqs. (8) and (9) [35].

$$Sk_p = \frac{1}{n} \sum_{i=1}^n \left(\frac{X_i - \mu}{\sigma^2} \right)^3 \quad (8)$$

$$K_p = \frac{1}{n} \sum_{i=1}^n \left(\frac{X_i - \mu}{\sigma^2} \right)^4 \quad (9)$$

where σ^2 is the standard variation.

The skewness can be used to measure the asymmetry of the probability distribution of a random variable. When $Sk_p > 0$, it indicates that the frequency distribution is right-skewed. Conversely, if $Sk_p < 0$, the frequency distribution is left-skewed. When $Sk_p = 0$, it suggests that the frequency distribution is symmetrical, meaning there is no skewness. Additionally, the kurtosis can reflect the steepness of the probability distribution of a random variable. If $K_p < 0$, the frequency distribution is sharp. When $K_p > 0$, it is a flat distribution, and the more the frequency distribution approaches a normal distribution when its values are closer to 0.

(2) Gamma distribution function

The Gamma distribution is a fundamental continuous probability distribution in probability theory and statistics [35]. Its probability density function (PDF) is defined by two parameters: the shape parameter ($\alpha > 0$) and the scale parameter ($\beta > 0$), and is given as follows for ($X \sim \Gamma(\alpha, \beta)$) [35]:

$$f(x; \alpha, \beta) = \frac{x^{\alpha-1} e^{-x/\beta}}{\beta^\alpha \Gamma(\alpha)} \quad (x > 0) \quad (10)$$

where α and β can be estimated for sample data using the following expressions [35]:

$$\alpha = \frac{\bar{x}}{\beta} - 1 \quad (11)$$

$$\beta = \frac{\sigma^2}{\bar{x}} \quad (12)$$

The gamma distribution is typically right-skewed, and its shape varies with the values of α and β . As the shape parameter (α) increases, the distribution becomes steeper and more symmetric. Conversely, increasing the scale parameter (β) results in a flatter, more spread-out curve.

4.2.2. Frequency distribution of asperity height

The fracture surface morphology was reconstructed from high-resolution point cloud data using MATLAB, as shown in Fig. 8. The surface was then discretized into a structured grid with element dimensions of 0.01 mm (X-axis) \times 0.02 mm (Y-axis), where each grid node stores spatial coordinates (X, Y, Z) within a Cartesian reference frame. The Z-coordinate represents the local asperity height (h), corresponding to the out-of-plane deviation of the crack surface from a nominal reference plane, and is readily obtained from the data [28,29]. To improve computational efficiency and avoid redundant data collection, only one crack surface was scanned based on the assumption that the opposing surfaces of a fractured specimen are topographically complementary. This assumption is justified by the nature of the fracture process, which typically produces conjugate surfaces with correlated roughness profiles. The resulting digital elevation model quantitatively represents surface asperities, forming the basis for subsequent statistical analysis of fracture roughness.

Fig. 12a Shows the frequency distribution histograms for asperity heights under various bedding angles. while the height distribution generally resembles normal distributions, notable differences across bedding angles reflect the strong coupling between macroscopic failure patterns and morphology evolution during crack propagation. Analysis of skewness (Sk_p) reveals that the 0° and 90° specimens have values predominantly between -0.3 and 0.5, indicating near-symmetrical height distributions. These surfaces exhibit moderate undulations, with limited prominent protrusions or depressions, corresponding to predominantly tensile failures. In contrast, the 30° specimen displays significantly higher variability; for instance, the 30°-4 specimen exhibits

a skewness of 1.57, indicating a pronounced right skew. These suggest a surface dominated by lower asperities interspersed with sharp, localized peaks and characterized complex fracture processes governed by bedding-induced deflection and a mixed I-II shear-tensile failure mechanism. The 60° specimen exhibits both positive (e.g., 60°-1, $Sk_p = 0.96$) and negative skewness (e.g., 60°-2, $Sk_p = -0.38$), reflecting alternating dominance of shear and tensile failure mechanisms and a more unstable crack propagation path. These findings are consistent with macroscopic failure patterns shown in Fig. 6 and Table 3.

Kurtosis (K_p) further characterizes the concentration of asperity height values. Most specimens have kurtosis values near 3.0, approximating a normal distribution and indicating moderate surface toughness. However, the 30°-4 specimen exhibits an exceptionally high kurtosis of 3.95, implying sharp protrusions and steep local structures. This feature is typically associated with stress concentration, transgranular fractures, or relative bedding plane displacements, reinforcing that a critical angle for enhanced fracture complexity. For 60° specimens, kurtosis values slightly below 1.0 (e.g., 60°-1, $K_p = 0.96$) indicate moderate roughness influenced by heterogeneous structural interfaces. Hence, the joint distribution of skewness and kurtosis provides further insight into the link between macro-morphology and failure mechanisms. Specimens with high skewness and kurtosis typically display rough, structurally complex, and frictionally dominated surfaces, indicative of mixed-mode failure. Conversely, specimens with skewness near zero and moderate kurtosis are associated with smoother, tensile-dominated failure. The 60° specimens represent a transitional state, with moderate roughness and instability in crack path evolution, reflecting a shift from tensile to shear-dominated propagation.

To further investigate the geometric undulation characteristics of fracture surfaces, this study analyzed key parameters, including the maximum values, minimum values, and standard deviation of asperity height, as shown in Fig. 12(b). The 30° specimens exhibiting markedly increased roughness and geometric heterogeneity. The maximum asperity height in the 30° specimens significantly exceeds that of other conditions, with an average value over 5.0 mm and a broad distribution range, indicating prominent local protrusions. In contrast, the maximum asperity height for 0°, 60°, and 90° specimens is below 2.5 mm, suggesting more regular crack propagation paths and reduced surface undulation. This observation reinforces the conclusion that 30° represents a critical range for fracture complexity, where cracks are more prone to deflection and local energy concentration.

The distribution of minimum asperity heights follows a similar trend. For the 30° specimens, local depressions reach depths of -8.0 mm, highlighting deep concave features. These suggest that crack propagation is more susceptible to bedding-induced asymmetry, forming uneven fracture surfaces with extreme height variations. By contrast, the 0°, 60°, and 90° specimens exhibit narrower minimum asperity height ranges, indicative of smoother, tensile, or shear-dominated crack propagation paths.

Roughness dispersion, measured by the standard deviation of asperity heights, further underscores these differences. The 30° specimens show the highest average standard deviation (close to 2.0), indicating pronounced surface irregularity. This complex micro-rough structure not only signifies uneven energy release during fracture but may also significantly influence interfacial contact behavior and macroscopic shear performance. The 90° specimens follow, while the 0° specimens exhibit the lowest standard deviation, showing the most consistent and regular surface morphology.

Fig. 13 systemically presents the variation trends of fractal dimension and the standard deviation of asperity height across different bedding angles. The results demonstrate a strong consistency in the variation patterns of both parameters across most specimens. Specifically, in the 30° and 90° specimens, both the standard deviation and fractal dimension increase markedly, indicating that as the complexity of the crack propagation path intensifies, the amplitude of surface height fluctuations increases in tandem with the geometric roughness and self-

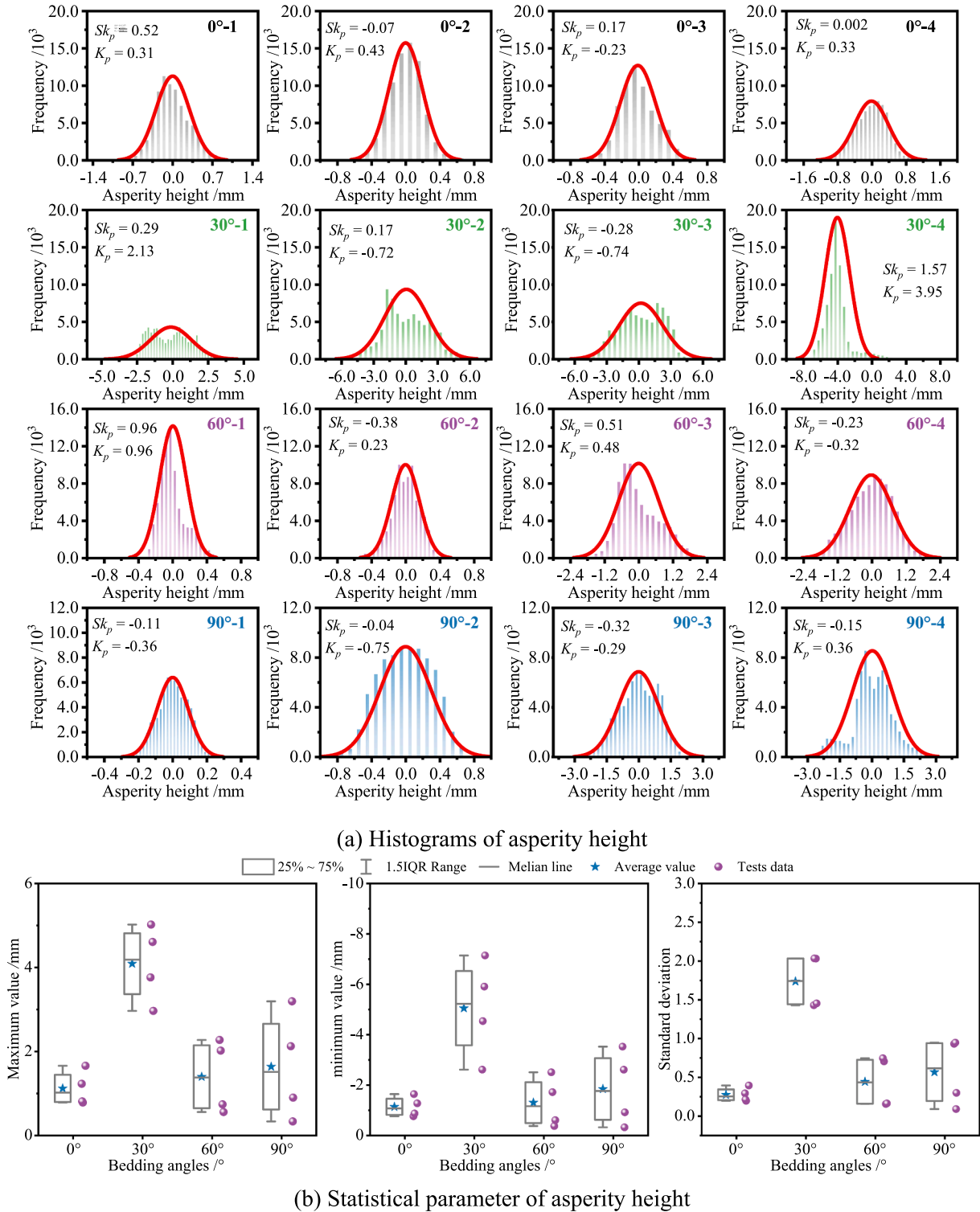


Fig. 12. Asperity height of fracture surfaces with different bedding angles.

similarity. This alignment suggests a close coupling between macroscopic failure behavior and morphology characteristics. Although slight fluctuations are observed in individual specimens (such as 0° and 60°), the overall trends of the two parameters remain highly synchronous. For example, the standard deviation in 60° specimens increases from approximately 0.2 to 0.75, while the fractal dimension rises from 2.11 to 2.23.

This finding confirms that standard deviation quantifies the magnitude of surface height variation, fractal dimension captures the

structural complexity and self-similar properties of the surface morphology. Their synchronous variation across multiple bedding angles reinforces their applicability and physical significance in quantitatively evaluating fracture surface roughness.

4.2.3. Frequency distribution of slope angles

Let the coordinate of a point on the crack surface element be denoted as $(X(i, j), Y(i, j), Z(i, j))$. The three-dimensional direction vectors along the X- and Y-axis directions are defined as [28,29]:

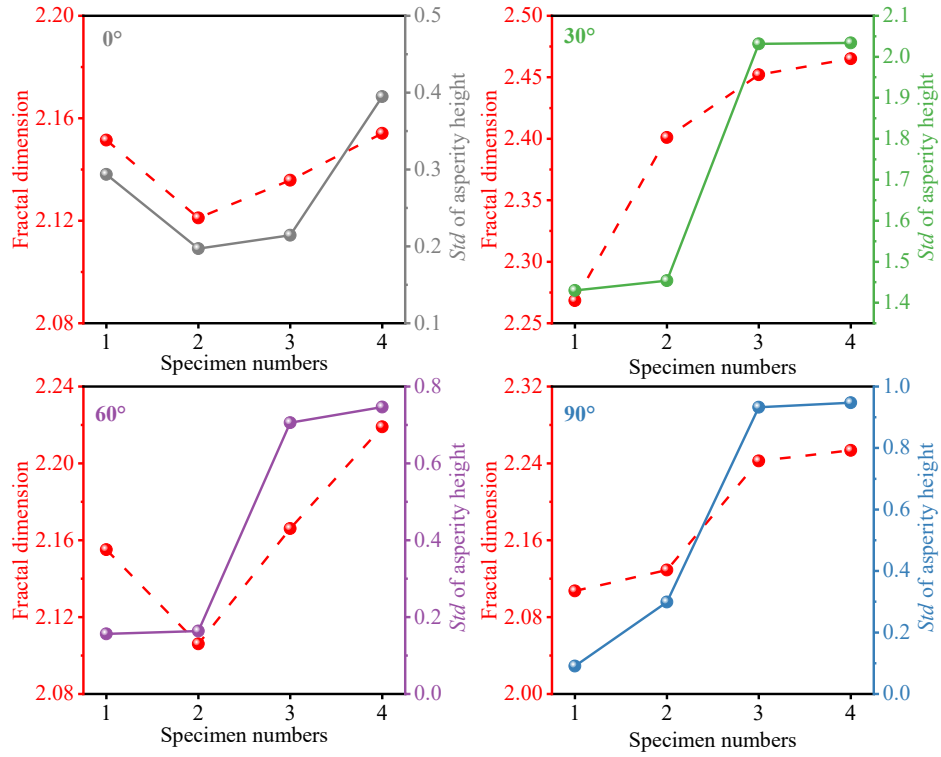


Fig. 13. Relationship between the fractal dimension and the standard deviation of asperity height with different bedding angles.

$$\begin{cases} \vec{p}_x = [X(i,j), Y(i,j), Z(i,j)] - [X(i+1,j), Y(i+1,j), Z(i+1,j)] \\ \vec{p}_y = [X(i,j), Y(i,j), Z(i,j)] - [X(i,j+1), Y(i,j+1), Z(i,j+1)] \end{cases} \quad (13)$$

The surface normal vector at each element can be calculated as the normalized cross product these two vectors:

$$\vec{c} = \frac{\vec{p}_x \times \vec{p}_y}{\|\vec{p}_x \times \vec{p}_y\|} \quad (14)$$

The slope angle (α_{sa}) is defined as the angle between the surface normal vector of the global Z-axis direction vector $\vec{v} = (0, 0, 1)$, and is calculated as Eq. (15). This slope angle characterizes the local inclination of the fracture surface at each element [28,29].

$$\alpha_{sa} = \cos^{-1}(\vec{c} \times \vec{v}) \quad (15)$$

Fig. 14(a) illustrates the frequency distribution and fitting results of the slope angle under different bedding angles using normal and gamma distribution models. The 30° specimens exhibit approximately normal distribution, with slope angles broadly distributed across the full range of 0° to 90°. The skewness is close to 0.0, and the kurtosis is negative, suggesting a symmetrical distribution with a relatively flat peak. Although the concentration of slope angle in 30° specimens is low, the wide angular range reflects pronounced angular variability and geometric irregularity, indicative of more complex surface morphology and enhanced roughness. By contrast, several representative specimens from 0°, 60° and 90° specimens (e.g., 0°-2, 60°-1 and 90°-2) align more closely with gamma distributions. Their frequency curves clear right-skewed trends, with slope angles predominantly concentrated in the low-to-medium range. These specimens exhibit steep frequency peaks and narrower distribution spans, suggesting fracture surfaces composed of densely distributed small-angle asperities with localized protrusions and lower roughness.

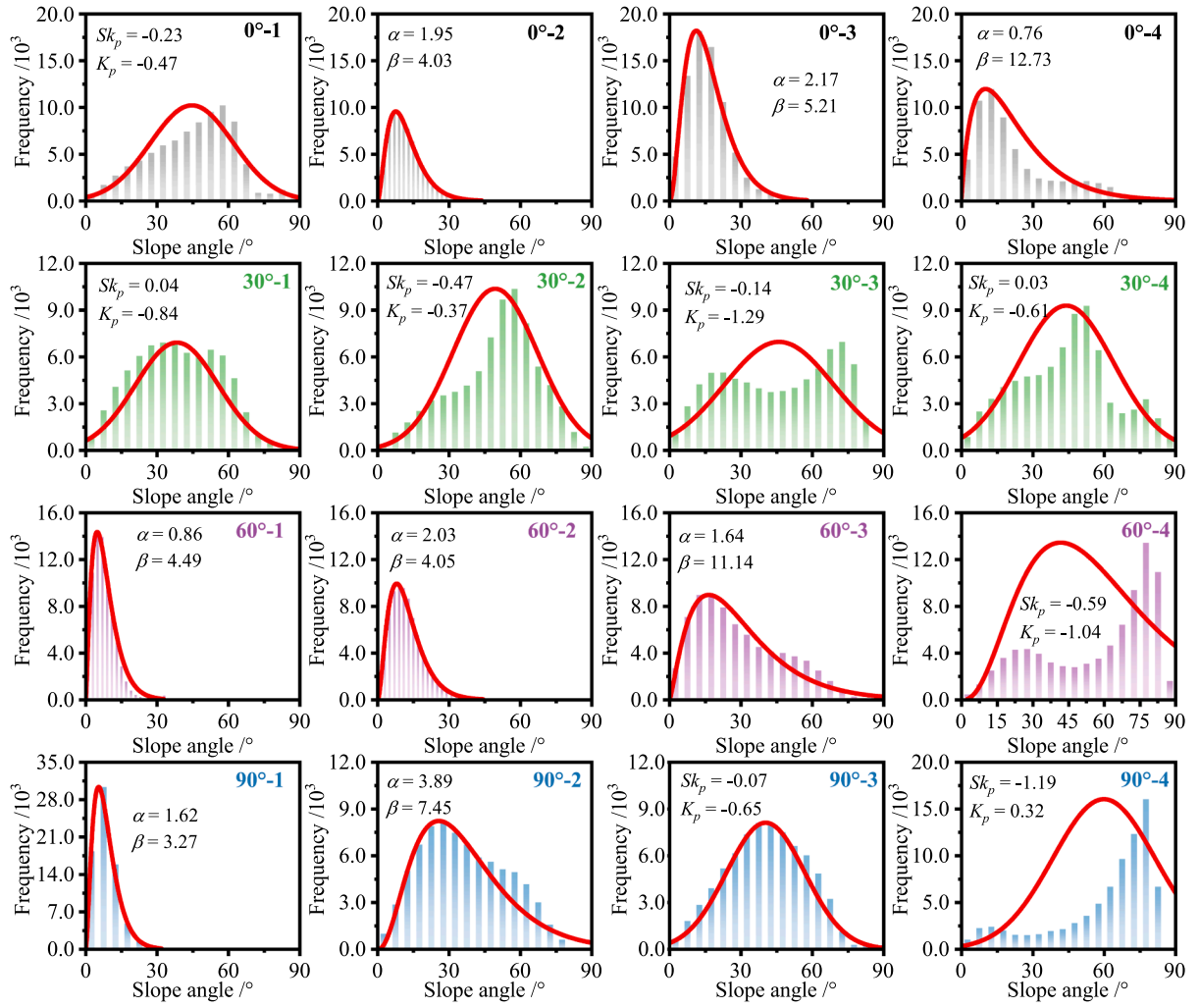
For 60°-1 specimen, with shape $\alpha = 0.86$ and the scale parameter $\alpha = 4.49$, the fitted curve is steep with a peak near 10°, indicating a surface dominated by low-angle features and relatively uneven geometry. In contrast, the 60°-3 specimen has $\alpha = 1.64$ and $\alpha = 11.14$, producing a

flatter distribution cover with a broader angular range, reflecting greater slope variability and a rougher surface. These observations are consistent with the failure patterns in Fig. 6 and Table 2.

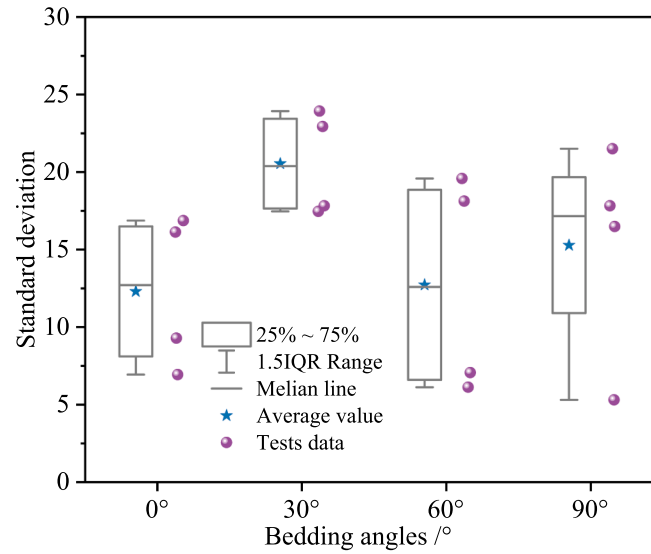
Although the 30° specimen mainly exhibits normal distributions, it generally shows higher fractal dimensions, showing more pronounced surface roughness. These suggest an important insight: The type of the slope angle distribution along (normal or gamma) does not directly determine surface roughness. While normal distribution indicates symmetry, they may also involve various slope variations, reflecting multi-scale undulations and complex surface geometries. Conversely, gamma distribution may represent concentrated angular features that, despite being densely packed, result in relatively lower localized shear or tensile surface roughness. Therefore, the distribution type and the extent of slope variation must be considered when evaluating fracture surface roughness rather than relying on a single metric. These insights provide theoretical and practical significance for understanding fracture behavior and modeling fracture interfaces in rock masses.

Fig. 14(b) illustrates the statistical distribution of the standard deviation of the slope angle for various bedding angles, thereby assessing the discreteness and uniformity of micro-dip-angle variation. Pronounced differences emerge among bedding angle groups, revealing structural dependence. The 30° specimens exhibit the lowest standard deviation overall, shown by short box-plot height, a narrow interquartile range, and the absence of outliers. These suggest consistent slope-angle and a more regular micro-dip-angle distribution. Coupled with the findings in Fig. 14(a), in which this specimen follows a normal distribution and displays a higher fractal dimension, these results imply that despite the geometric complexity of the fracture surface, slope angle variability remains statistically stable.

Conversely, the 0°, 60°, and 90° specimens display much greater dispersion, evident from taller box plots, larger amplitude fluctuation, and frequent outliers, especially at 90°. This enhanced discreteness does not necessarily indicate greater surface roughness; instead, it primarily reflects statistical fluctuation arising from the coexistence of normal and gamma slope angle distributions within specimens sharing the same



(a) Histograms of the slope angle



(b) Standard deviation of the slope angle

Fig. 14. Slope angle of fracture surfaces with different bedding angles.

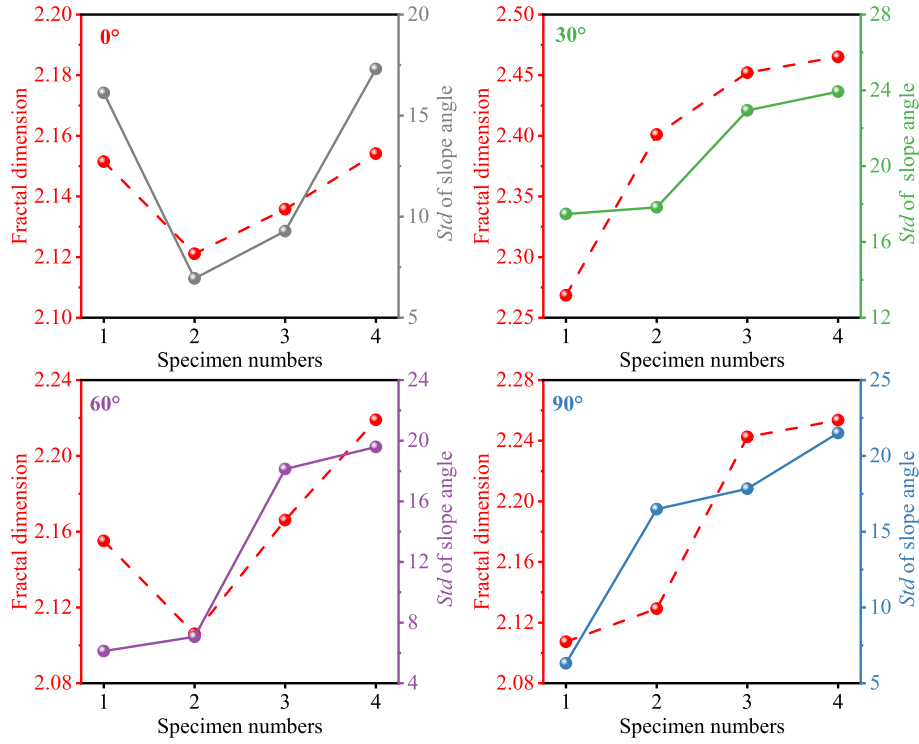


Fig. 15. Relationship between the fractal dimension and the standard deviation of slope angle with different bedding angles.

bedding angles. Some specimens show a wide, normally distributed range of slope angles, whereas others exhibit a gamma distribution concentrated at lower angles. The coexistence of these distribution patterns produces marked variability in the calculated standard deviation. Accordingly, the distribution of standard deviation values better captures the diversity of slope-angle distribution types than the intrinsic roughness of the fracture surface.

Fig. 15 presents the relationship between the fractal dimension and the standard deviation of slope angles. The results indicate that as the geometric roughness of the fracture surface increases, the dispersion of slope angles also grows significantly, suggesting a high degree of correlation between the two parameters during the evolution of the fracture surface. This trend is especially evident in the 30° and 90° specimens from No. 1 to No. 4 specimens. The fractal dimension steadily increases beyond 2.45, while the standard deviation of slope angles rises from approximately 13 to over 26. The nearly parallel change curves indicate a consistent and coordinated growth trend. These suggest that increased slope angle variability is closely linked to the development of multi-scale undulations on the fracture surface, reflecting the underlying microstructural evolution and complex interfacial morphology formation mechanism. Although slight fluctuations are observed in the 0° and 60° specimens, the overall positive correlation between fractal dimension and slope angle standard deviation remains robust. These findings further confirm that the standard deviation of slope angles effectively captures the local statistical complexity and self-similarity of the fracture surface.

4.2.4. Frequency distribution of aspect directions

The aspect direction (β_{ad}) represents the angle between the projection of the normal vector of each element on the XOY plane and the positive direction of the X-direction, which can be expressed as [28,29]:

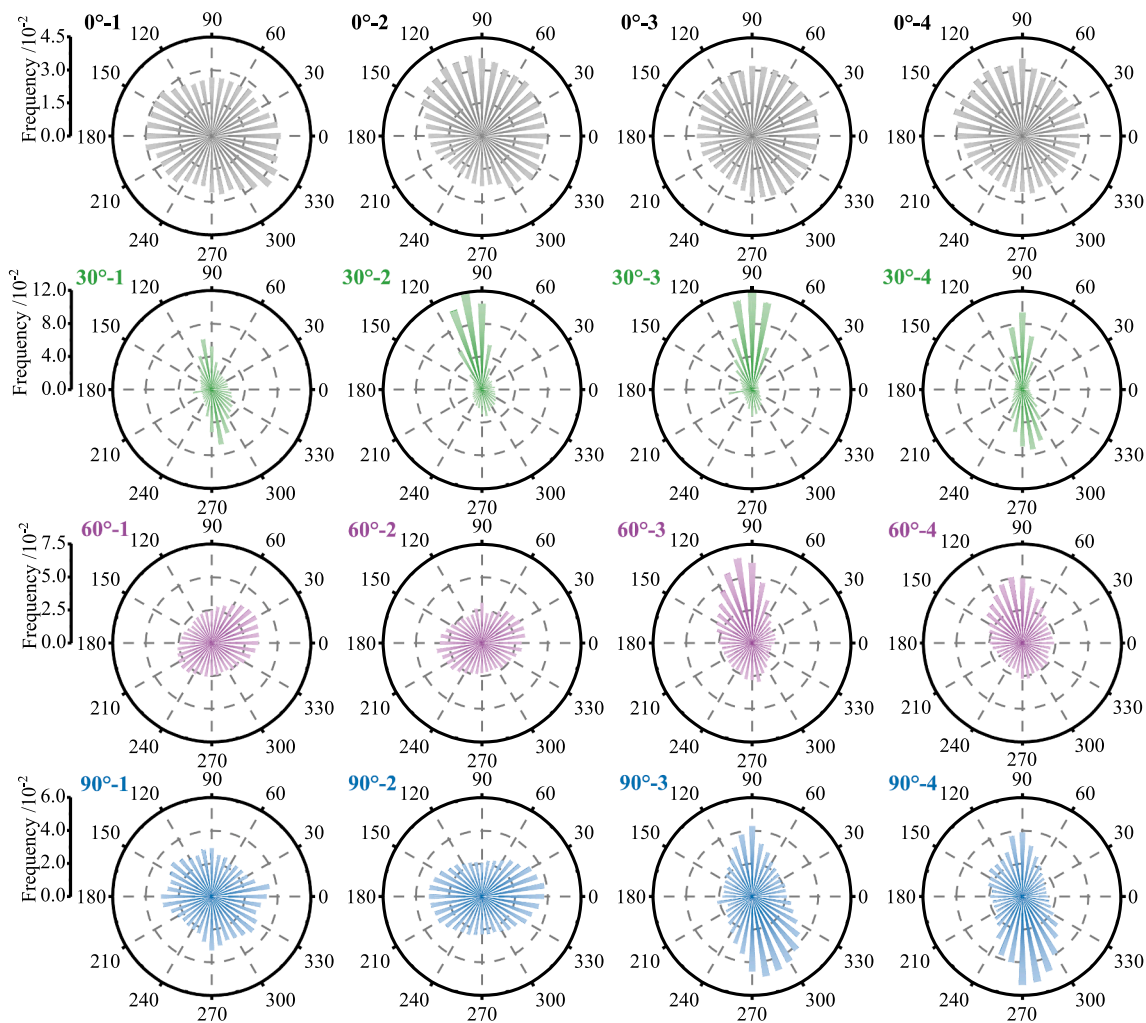
$$\beta_{ad} = \cos^{-1}(\vec{e}, \vec{u}) \quad (16)$$

where \vec{u} is the direction vector of the X axis (1, 0, 0), and \vec{e} is the projection vector of \vec{c} on the XOY plane.

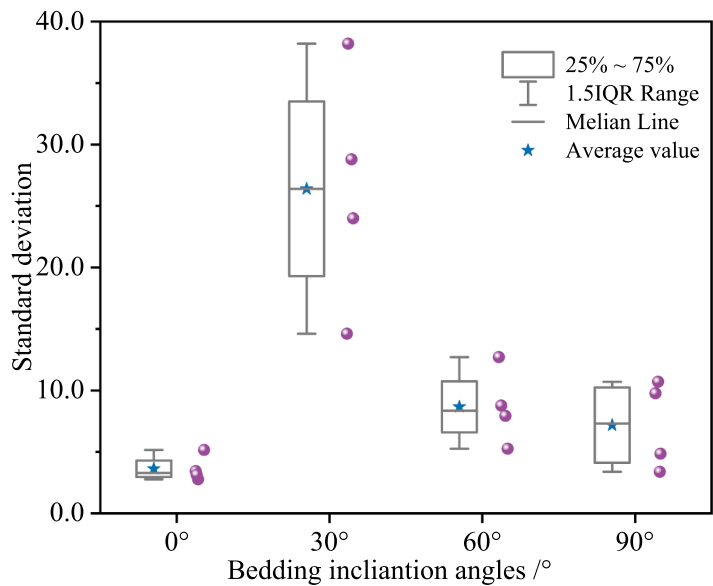
Fig. 16(a) shows the frequency distributions of aspect direction

under different bedding angles. For 0° specimens, the orientation angles almost uniformly spread over the full 360°, indicating no preferred direction and thus high spatial freedom of crack growth. This statistical characteristic suggests that crack propagation path is controlled mainly by the Mode-I tensile failure across the bedding plane, and the bedding itself exerts little morphology, producing a weakly anisotropic surface. By contrast, the 30° specimens exhibit the strongest anisotropy. Orientation cluster tightly with $270^\circ \pm 15^\circ$, forming a pronounced peak and a banded pattern in polar coordinates. This directional bias shows that crack advance is governed by the bedding planes, with bedding-guided sliding coupled to tensile failure. Such coupling failure pattern generates a complex, comparatively rough fracture surface (as shown in Fig. 6). The 60° and 90° specimens are intermediate, exhibiting moderate directional concentration atop a multi-directional background. The 60°-3 and 60°-4 specimens reveal a dominant trend yet retain secondary orientations, suggesting bedding guidance accompanied by deflection and disturbance; the resulting fractures correspond to Mode-I tensile failure across the bedding plane. Moreover, the 90°-3 and 90°-4 specimens display a mild peak near 270° , indicating that even under Mode-I tensile failure parallel to bedding plane, local bedding plane still impacts some directional control. Hence, the distribution characteristics of aspect direction on the fracture surface capture the degree of microscopic anisotropy and its governing mechanisms. A highly concentrated orientation spectrum signals strong bedding plane control. In contrast, a dispersed spectrum reflects greater influence from tensile failure across the bedding plane or shear failure along the bedding plane. These findings provide critical insight into the fracture evolution of shale.

Fig. 16(b) displays the standard deviation of the aspect direction under different bedding angles. The results indicate that the 30° specimens exhibit significantly higher standard deviations than other bedding angles. The box plot shows the greatest height and widest dispersion range, indicating a highly uneven orientation angle distribution with a strong directional concentration. These suggest that the bedding plane exerts substantial control over crack propagate, resulting in increased crack path instability. These findings align closely with the directional characteristics observed in the polar coordinate plots, as



(a) Frequency distributions of the aspect direction



(b) Standard deviation of the aspect direction

Fig. 16. Aspect direction of fracture surfaces under different bedding angles.

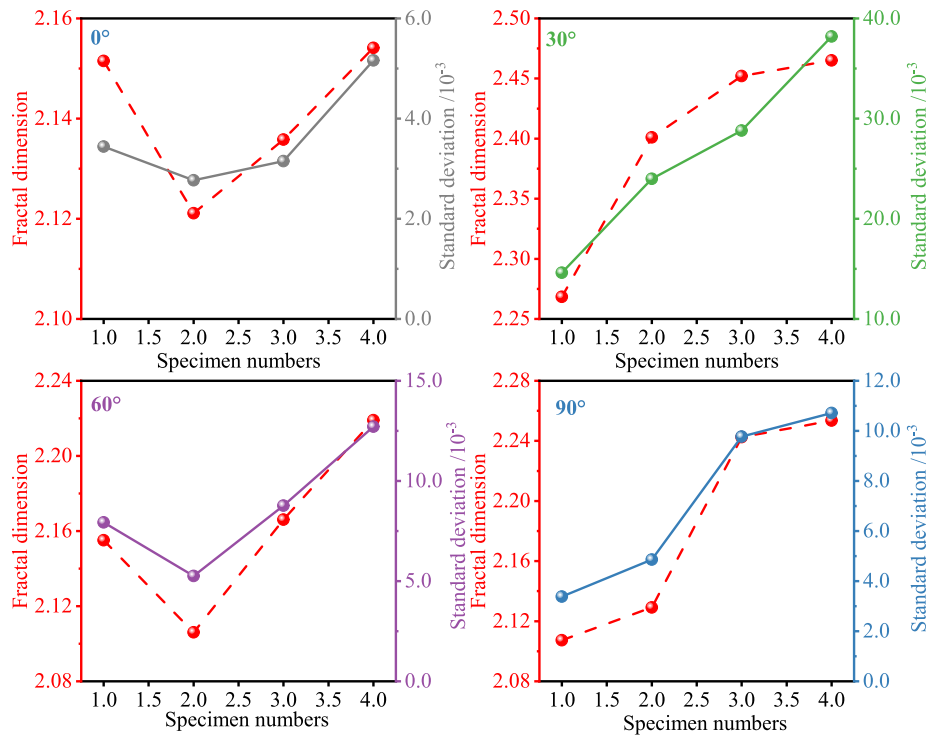


Fig. 17. Relationship between fractal dimension and standard deviation of the aspect direction with different bedding angles.

shown in Fig. 16(a). In contrast, the 0° specimens show the lowest standard deviation, indicating a more uniform orientation angle distribution. These reflect minimal influence from the bedding plane on crack propagate and suggest a higher level of path stability. The standard deviations for 60° and 90° specimens fall between these extremes, showing moderate directional dispersion and propagation disturbance.

These results imply that cracks are partially guided by the bedding plane under these conditions while maintaining a certain degree of propagation freedom.

Fig. 17 illustrates the relationship between fractal dimension and standard deviation of the aspect direction with different bedding angles. Overall, the two parameters exhibit strong synchronous growth trends

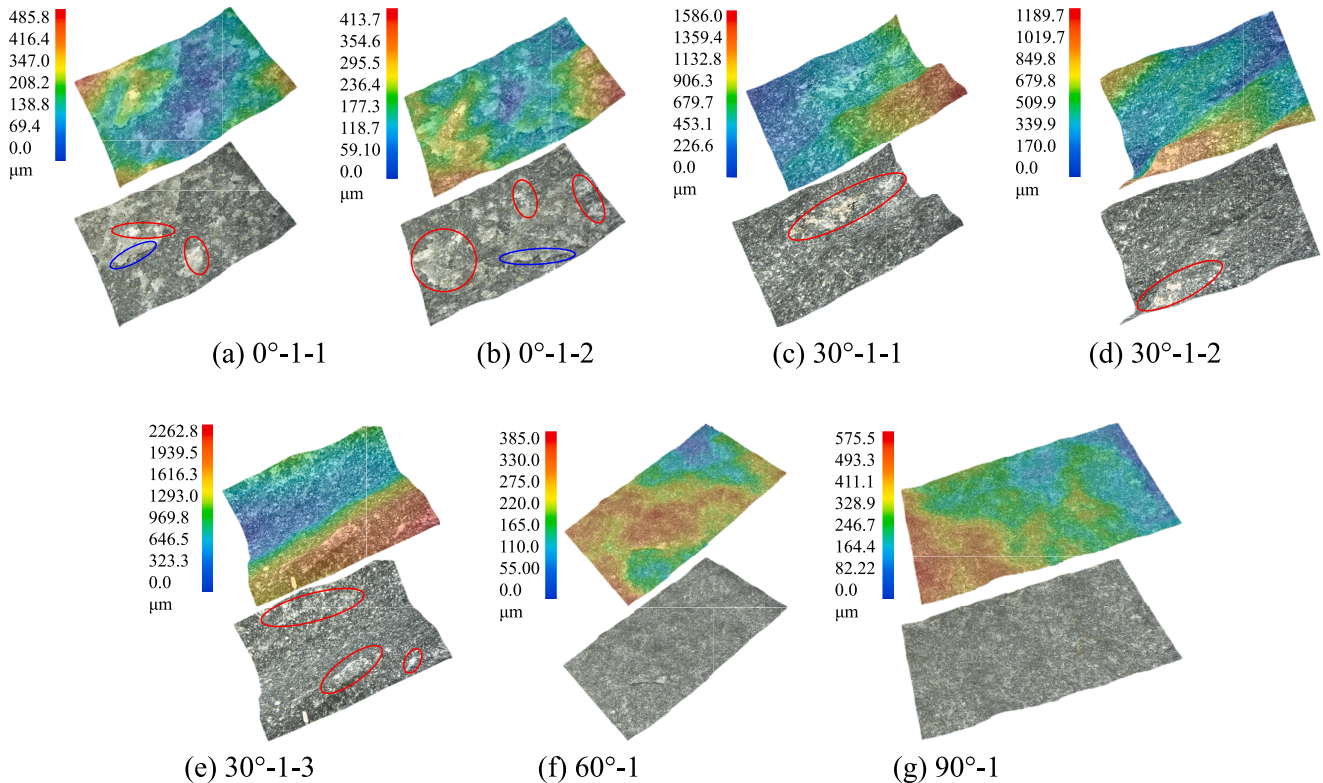


Fig. 18. The fracture surface of ultra-depth field microscopy morphology with various bedding angles ($\times 200$).

across most specimens, indicating a high degree of consistency in their variation. These results suggest that greater geometric complexity of the fracture surface is associated with more pronounced directional deviation in its microstructure. This co-evolution implies that when the spatial arrangement of microscopic asperities becomes more intricate and the surface roughness increases, the non-uniformity of directional distribution similarly intensifies, reflecting enhanced structural anisotropy. The standard deviation of the aspect direction effectively captures the discreteness of microstructure directionality. Its strong correlation with the fractal dimension indicates that it can serve as a valuable auxiliary parameter for assessing microstructural disturbances and the evolution of fractal characteristics.

In conclusion, relying on a single indicator is inadequate to fully capture the complexity and multi-scale characteristics of crack geometry. By jointly analyzing parameters, such as asperity heights, slope angles, aspect direction, and their corresponding statistics (such as standard deviation, skewness, kurtosis, shape parameter, and scale parameter, etc.), the structural evolution and primary control mechanisms governing crack propagation process can be more systematically understood.

4.3. Surface morphology for ultra-depth field microscopy system

Section 4.2 systematically examined the macroscopic morphology characteristics of fracture surfaces under different bedding angles. However, the mesoscopic morphology is equally critical for understanding their fracture mechanism. Traditional optical microscopy, limited by a shallow depth of field, often fails to capture clear images of fracture surfaces with high undulations and irregular geometries, leading to information loss or geometric distortion. Non-flat features usually result in the loss of local information or geometric distortion. Ultra-depth field microscopy technology, equipped with a zoom optical

system, enables continuous, cross-scale observation from macroscopic to mesoscopic levels. This approach effectively overcomes the limitations of traditional imaging techniques and offers a robust tool for multi-scale, coupled analysis of fracture surface morphology.

Fig. 18 presents the ultra-depth field microscopic 3D topography and corresponding elevation cloud maps of the fracture surfaces under different bedding angles ($\times 200$). The elevation cloud maps reveal substantial differences in surface undulations, including complex meso-fracture structures. The overall surface elevation is relatively low, with height variations primarily in the range of 0—400 μm for 0° -1 specimen. The surface displays minor undulations and weak uniformity. In contrast, the 30° -1 specimen exhibits significantly enhanced surface roughness, with maximum elevations exceeding 2000 μm , forming highly irregular morphologies. The 60° -1 specimen shows moderate surface undulations, with elevations mostly between 200—500 μm and without abrupt transitions. The 90° -1 specimen demonstrates relatively balanced surface elevation, concentrated in the 100—600 μm range, suggesting moderate roughness. The results above further confirm that the 30° -1 specimen exhibits the highest surface roughness, and the subsequent analysis will employ 3D joint roughness coefficients (JRC) for quantitative characterization.

Additionally, the 3D morphology enables the examination of mesoscopic failure characteristics of mineral crystals, providing insights into fracture mechanisms for various bedding angles. As shown in Fig. 18(a)-(b) (0° -1 specimen), delamination is observed at grain boundaries in the blue-elliptical region, where crystals separate along relatively flat cleavage planes. These indicate crack propagation primarily along grain boundaries driven by normal tensile stress. Concurrently, distinct frictional marks are evident in the red-elliptical regions, suggesting local shear force influence and partial shear failure components. For 30° -1 specimen (as shown in Fig. 18(c)-(e)), red-elliptical regions are widespread in regions of sharp elevation changes, where evident

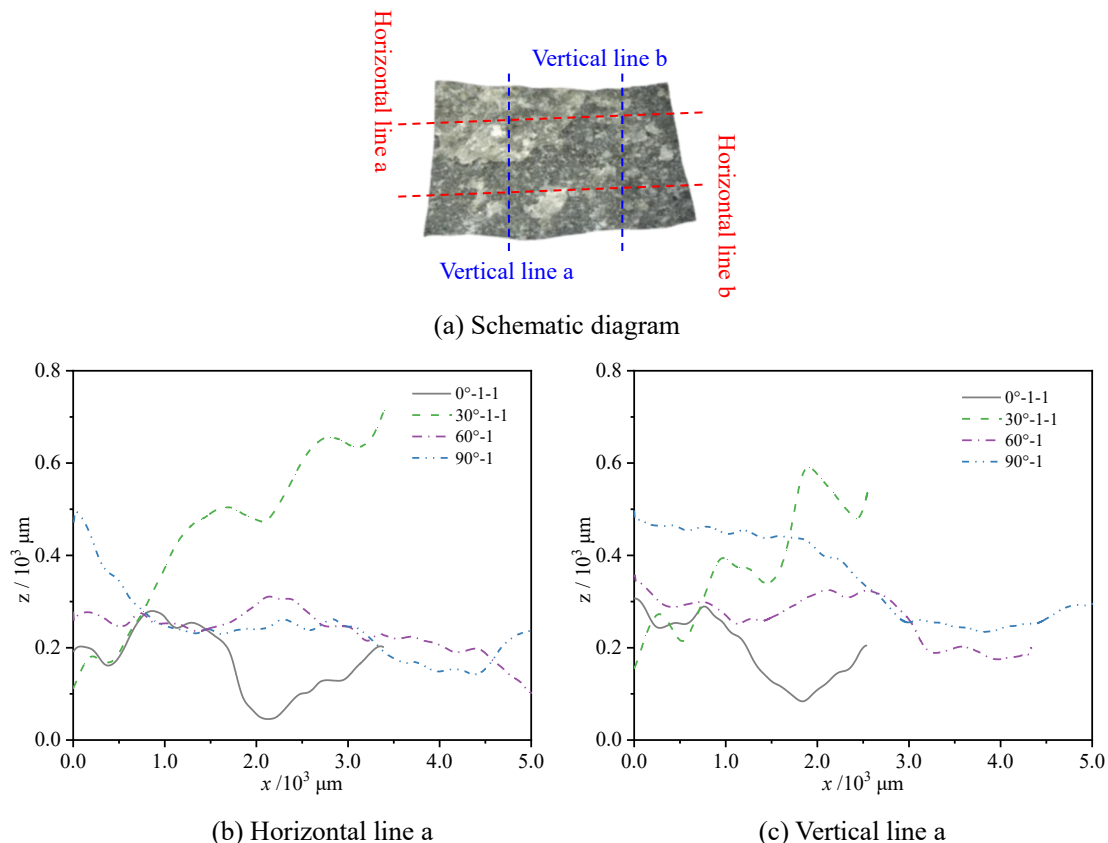


Fig. 19. Fracture surface profile for various bedding angles.

intergranular nesting, sliding, and dragging are observed. These characteristics indicate a dominant shear component with strong frictional sliding and displacement between grains. This results in the formation of localized shear micro-crack, propagating along the weak sliding surfaces—a hallmark of tensile-shear coupled failure. This complex energy dissipation process contributes to the high fractal dimension and corresponds with the extreme local elevation values, reinforcing the interpretation of 30° as a tensile-shear cooperative failure. As shown in Fig. 18(f), no significant grain displacement or delamination is observed in the 60° -1 specimen. The crack propagation path appears relatively smooth, with a combined mechanism of intergranular sliding and localized micro-peeling. The overall structure remains continuous, indicating a shear-dominated yet stable fracture mode. For 90° -1 specimen (as shown in Fig. 18(g)), long-range sliding traces are absent. This suggests that crack propagation is primarily controlled by tensile stresses, with only limited microstructural undulations present in locally weak regions.

Fig. 19 presents the elevation distribution curves along the horizontal and vertical profile lines extracted from the ultra-depth field microscopic images, providing a quantitative assessment of the meso-scale undulation behavior of fracture surfaces. Fig. 19(a) shows the schematic diagram of the profile line extraction positions. The 30° -1 specimen exhibits the most pronounced elevation fluctuations in both directions. The profile curves display sharp undulations and significant peak-to-valley differences, indicating the presence of numerous surface protrusions and deep depressions. These characteristics reflect the highest geometric complexity and higher rough fracture surface, substantiating that 30° represents the critical bedding angle for complex fracture evolution. In contrast, the 0° -1 specimen shows a relatively low overall elevation, with smooth profile curves and maximum values not exceeding $0.3 \times 10^3 \mu\text{m}$. These indicate a limited surface undulation amplitude and a crack propagation process primarily governed by tensile mechanisms, with minimal influence from bedding planes. The 60° -1 specimen demonstrates moderate elevation variation, with noticeable undulations in the profile curve but a restricted overall amplitude, showing a moderately undulating surface morphology. The 90° -1 specimen exhibits a relatively smooth and continuous elevation curve with higher elevation values despite a smaller undulation amplitude, showing a uniformly uplifted fracture surface. The phenomenon may be attributed to the combined effect of controlled interlayer slip and weak local disturbance during crack propagation parallel to the bedding plane.

The JRC for a 2D profile line can be calculated by Eq. (17) [36]:

$$\text{JRC} = 32.20 + 32.47 \lg Z_2 \quad (17)$$

where Z_2 is the root mean square of the first derivative of the profile line, which can be calculated by Eq. (18) [27,29,37].

$$Z_2 = \sqrt{\frac{1}{M} \sum_{i=1}^M \left(\frac{z_{i-1} - z_i}{x_{i-1} - x_i} \right)^2} \quad (18)$$

where x_i and z_i are the coordinates of the profile line, and M is the points number of the profile line.

Fig. 20 shows the distribution characteristics of JRC values along the horizontal and vertical directions. This analysis seeks to evaluate the scale-dependent characteristics of the micro-geometric undulations on fracture surface. In both measurement directions, the 30° -1 specimen exhibits significantly higher JRC values than other bedding angles, with average values of approximately 15.0 in the horizontal direction and 17.0 in the vertical direction. The maximum JRC of 30° -1 specimen exceeds 18.0, indicating pronounced surface roughness characterized by well-developed micro-protrusions and grooves, and a marked increase in structural complexity. In contrast, the 0° -1, 60° -1, and 90° -1 specimens exhibit considerably lower JRC values, reflecting a generally smoother fracture surface. Among these, the 90° -1 specimen shows the lowest roughness, with average JRC values ranging from 3.0 to 8.0. These suggest minimal surface undulation and limited geometric disturbance, a result closely linked to the loading direction parallel to the bedding plane, which promotes crack propagation along the stratification and leads to strong structural control but weak morphology complexity. These findings are consistent with the spatial undulation patterns observed in the elevation profiles presented in Fig. 19 and the fracture surface morphology shown in Fig. 18.

4.4. Micro-cracks and fracture characteristics by SEM

Microscopic examination of the shale was conducted using SEM devices ($\times 5000$), and the results are shown in Fig. 21. For 0° specimen (as shown in Fig. 21(a)), the fracture surface primarily exhibits large-scale flaky delamination structures, with fragmented particles distributed along the bedding plane. Crack propagation path is dominated by interlayer fracturing, with transgranular rupture observed. This micro-morphology indicates that when the loading direction is perpendicular to the bedding plane, cracks initiate and propagate along the inherent weak planes. The prevailing fracture mode is tensile cracking accompanied by interlayer delamination, with cracks mostly propagating along mineral boundaries. Energy is concentrated at the interfaces between adjacent grains, resulting in anisotropic delamination structures. The 30° specimens show the most complex fracture surface morphology,

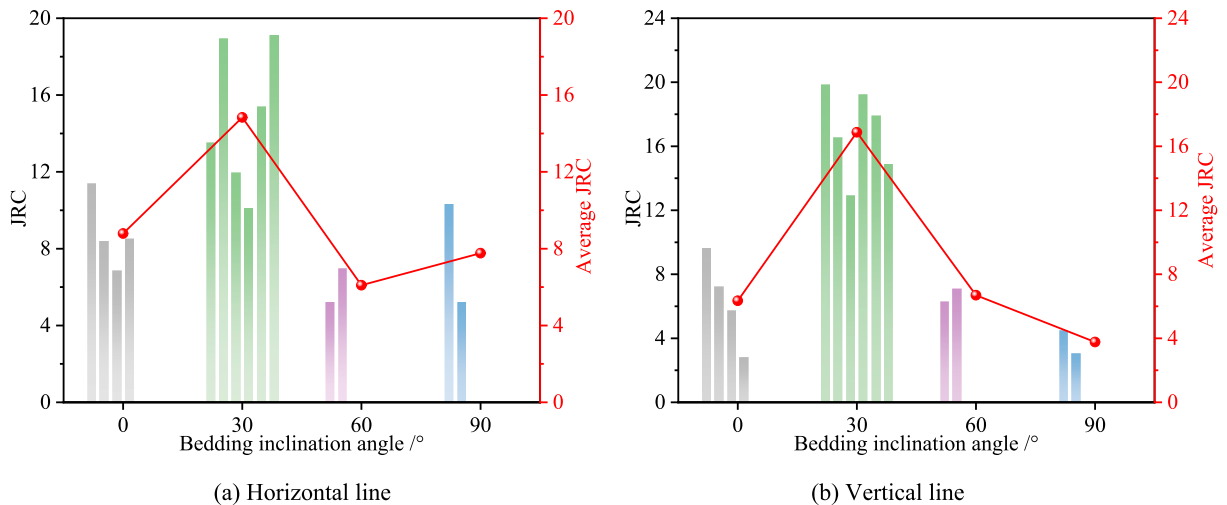


Fig. 20. JRC value for various bedding angles.

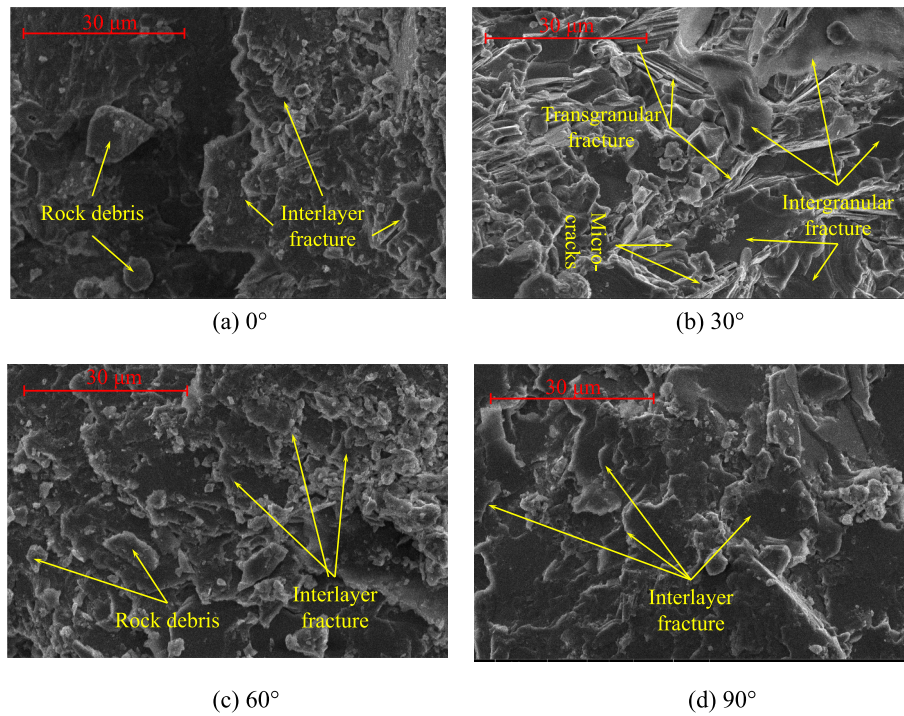


Fig. 21. SEM image for various bedding angles ($\times 5000$).

characterized by the synergistic evolution of multiple micro-fracture mechanisms (as shown in Fig. 21(b)). Alongside typical interlayer fracture and intergranular fractures, extensive transgranular fractures and interwoven micro-cracks are observed. These indicate that crack propagation path is governed by a coupled tension-shear mechanism, with localized regions of high energy concentration leading to direct grain penetration, resulting in a rough, highly heterogeneous fracture surface.

For 60° specimen (as shown in Fig. 21(c)), the fracture surfaces are primarily composed of interlayer delamination structures, with fine particles accumulated in localized regions. The overall surface appears compact, with closely arranged particles. Crack propagation path mainly follows the bedding planes, and the dominant fracture mode remains interlayer separation. However, shear-induced disturbances in certain regions give rise to slip-tear structures, indicating a transitional fracture mechanism between tensile and shear control. The number of micro-cracks is relatively low, the energy dissipation process is moderate, and the crack propagation path is relatively smooth and continuous. The 90° specimen also displays typical interlayer fracture characteristics, as shown in Fig. 21(d). The microstructure primarily comprises cleavage delamination and grain boundary cracking, with relatively smooth interfaces between mineral crystals. No significant evidence of transgranular tensile or shear failure is present. This surface morphology is consistent with macroscopic observations of crack propagate along the bedding plane, suggesting that the fracture process is dominated by tensile separation along bedding planes. Energy is primarily dissipated through weak-plane cracking and localized micro-delamination, resulting in a relatively mild fracture associated with low surface roughness and fractal dimension. Hence, the fracture surfaces microstructural under different bedding angles exhibit significant variability, revealing an evolution of fracture mechanisms from tensile-dominated to tensile-shear coupled modes. The 30° specimen represents a critical transitional configuration, showing the most complex morphology and intense fracturing behavior.

Previous studies on shale fracture surface morphology characteristics have primarily relied on fractal dimension [12,31,32], which, while effective in quantifying surface roughness, is limited in capturing the

spatial structure, scale-coupling features, and underlying mechanisms of fracture formations. This study employs a comprehensive multi-scale characterization framework that integrates ultra-depth-of-field microscopy, three-dimensional optical scanning, and scanning electron microscopy (SEM). This approach enables high-resolution observation of fracture surfaces across micrometer to millimeter scales, offering a more complete and realistic representation of fracture surface geometry.

Multi-scale fracture surface morphology is a key approach to understanding crack propagation mechanisms and fracturing performance during hydraulic fracturing. At the microscopic scale, features such as surface roughness, bifurcation behavior, and mineral composition influence stress concentration at the crack tip and govern propagation direction. At the mesoscopic scale, fracture network connectivity, distribution patterns, and interactions with bedding planes directly affect fracture complexity and effective flow capacity. At the macroscopic scale, fracture surface morphology determines the spatial distribution of the overall fracture zone and plays a decisive role in stimulated reservoir volume and production enhancement. Moreover, roughness and distribution patterns can inform the optimization of fracturing fluid viscosity, injection rate, and proppant concentration, promoting full fracture opening and improved conductivity. Identifying the dominant failure mechanism aids in optimizing perforation density and cluster spacing, thereby enhancing fracture network construction. In fracturing simulations, fracture surface morphology parameters can serve as inputs for fracture toughness, friction coefficient, and flow capacity, improving the accuracy of numerical predictions. Thus, multi-scale characterization enables a systematic understanding of fracture surface morphology evolution, providing valuable guidance for designing effective fracturing strategies in unconventional oil and gas reservoirs.

5. Conclusion

This study investigates how the bedding angle affects the fracture toughness, failure mechanisms, and fracture surface characteristics of shale specimens under the NSCB testing. The following conclusions can be summarized as follows:

(1) Peak load and fracture toughness decrease with increasing

bedding angle. The standard deviation and coefficient of variation also decline, indicating reduced data dispersion. At low bedding angles (e.g., 0° and 30°), it is more susceptible to interference from the bedding planes, leading to diverse failure modes and greater variability. At higher bedding angles (e.g., 60° and 90°), cracks propagate more stably along or across the bedding plane, dominated by interlayer separation, resulting in more consistent fracture mechanical behavior.

(2) The failure patterns can be divided into four types: tensile failure across the bedding plane (0°), shear failure along the bedding plane with mixed failure across the bedding plane (30°), shear failure along the bedding plane or tensile failure across the bedding plane (60°), and tensile failure along the bedding plane (90°). Interlayer fracture is the predominant failure mode, resulting in relatively smooth fracture surfaces (0°, 60°, and 90°). The 30° specimens display the most complex tensile-shear coupling failure characteristics, marked by rough fracture surfaces and maximum energy dissipation.

(3) Deformation characteristics in the compaction stage vary with bedding angles, indicating different failure mechanisms. Specimens failing across the bedding plane or by mixed patterns (e.g., 0°, 30°, 60°-3 and 60°-4) show a pronounced concave curve due to early microcrack development and gradual energy release. Specimens failing along the bedding plane (e.g., 90°, 60°-1, and 60°-2) show a more direct response, with crack propagation requiring less energy, highlighting the bedding plane's dominant role.

(4) The fractal dimension first increases and then gradually decreases with the increases of the bedding angle. The 30° specimens exhibit the highest fractal dimension and greatest variability, indicating the most complex fracture paths and the strongest influence from bedding plane. The 0° specimens display the most stable fracture surfaces, while the 60° and 90° specimens show moderate and slightly higher variations, reflecting diverse failure mechanisms.

(5) The asperity height generally conforms to a normal distribution, while the slope angle can be fitted by either a normal or gamma distribution. Fracture surfaces following a normal distribution of slope angle exhibit higher roughness. A more even aspect direction distribution corresponds to reduced geometric undulation and lower surface roughness. The standard deviations of asperity height, slope angle, and aspect direction all show strong correlations with the fractal dimension, indicating that these statistical parameters effectively capture the fracture morphology. The JRC value is also consistent with the morphology results, showing that the 30° specimens are the roughest.

CRedit authorship contribution statement

Zhuo Dong: Writing – review & editing, Supervision, Funding acquisition. **Xiaoyan Zhai:** Writing – original draft, Investigation, Conceptualization. **Yingxian Lang:** Writing – review & editing, Funding acquisition. **Bin Gong:** Writing – review & editing, Supervision, Funding acquisition. **Ruifu Yuan:** Methodology. **Zhuli Ren:** Funding acquisition.

Declaration of competing interest

The authors declare that they have no known competing financial interests or personal relationships that could have appeared to influence the work reported in this paper.

Acknowledgments

The authors would like to acknowledge the financial support from the National Natural Science Foundation for Young Scientists of China (Grant No. 52104084), the Science and Technology Tackling Project of Henan Province, China (Grant No. 252102321155, 252102321101), the China Postdoctoral Science Foundation, China (Grant No. 2024M760807), and the UK Research and Innovation, UK (Grant No. EP/Y02754X/1).

Data availability

Data will be made available on request.

References

- [1] Y. Guo, L. Huang, X. Li, Experimental and numerical investigation on the fracture behavior of deep anisotropic shale reservoir under in-situ temperature, *Energy* 282 (2023) 128969.
- [2] X. Liu, Z. Liang, S. Meng, C. Tang, J. Tao, Numerical simulation Study of Brittle Rock Materials from Micro to Macro Scales using Digital image Processing and Parallel Computing, *Appl. Sci.* 12 (8) (2022) 3864.
- [3] C. Zhao, J. Liu, C. Lyu, C. Liang, D. Xu, Y. Ren, Mechanical responses and failure characteristics of Longmaxi formation shale under real-time high temperature and high-stress coupling, *Eng. Fail. Anal.* 152 (2023) 107490.
- [4] C. Li, S. Zhong, H. Xie, C. Zhou, J. Hu, Microscopic time-dependent mechanical behavior of shale derived from nanoindentation, *Deep Underground Science and Engineering*, Online, doi: 10.1002/dug2.12143.
- [5] H. Lu, Y. Qi, W. Chen, C. Li, X. Li, Coupling effect of temperature and confining pressure on fracture toughness of transversely isotropic shale: Insights from a thermal-mechanical DEM model, *Rock Mechanics Bulletin* 4 (2025) 100211.
- [6] S. Heng, X. Liu, X. Li, X. Zhang, C. Yang, Experimental and numerical study on the non-planar propagation of hydraulic fractures in shale, *J. Petrol. Sci. Eng.* 179 (2019) 410–426.
- [7] W. Liang, J. Wang, C. Leung, S. Goh, S. Sang, Opportunities and challenges for gas coproduction from coal measure gas reservoirs with coal-shale-tight sandstone layers: A review, *Deep Underground Science and Engineering*. 4 (2025) 83–104.
- [8] R.M. Tuzingila, L. Kong, R.K. Kasongo, A review on experimental techniques and their applications in the effects of mineral content on geomechanical properties of reservoir shale rock, *Rock Mechanics Bulletin* 3 (2024) 100110.
- [9] Y. Duan, X.T. Feng, X. Li, B. Yang, Mesoscopic damage mechanism and a constitutive model of shale using in-situ X-ray CT device, *Eng. Fract. Mech.* 269 (2022) 108576.
- [10] Y. Guo, L. Huang, X. Li, Experimental investigation of the tensile behavior and acoustic emission characteristics of anisotropic shale under geothermal environment, *Energy* 263 (2023) 125767.
- [11] A. Zhang, R. Zhang, H. Lu, Z. Yang, Z. Zhang, L. Ren, Anisotropy in shear failure of shale: an insight from microcracking to macrorupture, *Measurement* 243 (2025) 116391.
- [12] Y. Li, Y. Hu, H. Zheng, Influence of bedding on fracture toughness and failure patterns of anisotropic shale, *Eng. Geol.* 341 (2024) 107730.
- [13] K. Zheng, Y. Zhao, C. Wang, J. Bi, Influence of distinct testing methods on the mode-I fracture toughness of Longmaxi shale, *Theor. Appl. Fract. Mec.* 129 (2024) 104213.
- [14] B. Lei, J. Zuo, H. Liu, J. Wang, F. Xu, H. Li, Experimental and numerical investigation on shale fracture behavior with different bedding properties, *Eng. Fract. Mech.* 247 (2021) 107639.
- [15] J. Hu, H. Xie, Q. Sun, C. Li, G. Liu, Changes in the thermodynamic properties of alkaline granite after cyclic quenching following high temperature action, *Int. J. Min. Sci. Techno.* 31 (5) (2021) 843–852.
- [16] V. Vishal, M. Rizwan, B. Mahanta, S.P. Pradhan, T.N. Singh, Temperature effect on the mechanical behavior of shale: Implication for shale gas production, *Geosystems and Geoenvironment*. 1 (4) (2022) 100078.
- [17] X. Shi, Y. Zhao, S. Gong, W. Wang, W. Yao, Co-effects of bedding planes and loading condition on Mode-I fracture toughness of anisotropic rocks, *Theor. Appl. Fract. Mec.* 117 (2022) 103158.
- [18] Z. Yan, L. Wang, J. Jin, J. Wang, Dynamic properties of mode I and mode II fractures of shale under impact loading, *J. Rock. Mech. Geotech.* 17 (2) (2025) 1053–1067.
- [19] H. Wang, T. Ma, Y. Liu, D. Zhang, P.G. Ranjith, Experimental Investigation on the 3D Anisotropic Fracture Behavior of Layered Shales under Mode-I Loading, *Rock Mech. Rock Eng.* 57 (2024) 3459–3482.
- [20] T. Ma, H. Wang, Y. Liu, C. Fu, R.G. Ranjith, Experimental investigation on the anisotropy of mode-I fracture and tensile failure of layered shale, *Eng. Fract. Mech.* 290 (2023) 109484.
- [21] Z. Liu, H. Xu, Z. Zhao, Z. Chen, DEM Modeling of Interaction between the Propagating Fracture and Multiple Pre-existing Cemented Discontinuities in Shale, *Rock Mech. Rock Eng.* 52 (2019) 1993–2001.
- [22] S. Heng, X. Li, X. Liu, Y. Chen, Experimental study on the mechanical properties of bedding planes in shale, *J. Nat. Gas Sci. Eng.* 76 (2020) 103161.
- [23] M.L. Xiao, H.Q. Xie, G. Feng, Q. He, H.Z. Liu, L. Zhuo, Investigation on the fracture mechanics characteristics and crack initiation of deep dense shale, *Eng. Fract. Mech.* 301 (2024) 110039.
- [24] Y. Liu, D. Huang, D. Cen, Z. Zhong, F. Gong, Z. Wu, Y. Yang, Tensile Strength and Fracture Surface Morphology of Granite under Confined Direct Tension Test, *Rock Mech. Rock Eng.* 54 (2021) 4755–4769.
- [25] J. Ma, D. Li, S. Du, Z. Han, P. Luo, J. Zhao, Comparison of subcritical crack growth and dynamic fracture propagation in rocks under double-torsion tests, *Int. J. Rock. Mech. Min.* 170 (2023) 105481.
- [26] Z. Wang, H. Lian, W. Liang, P. Wu, W. Li, Y. Yu, D. Zhu, Experimental study on crack propagation characteristics of unconventional reservoir rocks, *Theor. Appl. Fract. Mec.* 131 (2024) 104335.

- [27] H. Zhou, Z. Liu, W. Shen, T. Feng, G. Zhang, Mechanical property and thermal degradation mechanism of granite in thermal-mechanical coupled triaxial compression, *Int. J. Rock. Mech. Min.* 160 (2022) 105270.
- [28] C. Zhang, D. Li, C. Wang, J. Ma, A. Zhou, P. Xiao, Effect of confining pressure on shear fracture behavior and surface morphology of granite by the short core in compression test, *Theor. Appl. Fract. Mec.* 121 (2022) 103506.
- [29] R. Cao, C. Wang, T. Hu, R. Yao, T. Li, Q. Lin, Experimental investigation of plane shear fracture characteristics of sandstone after cyclic freeze–thaw treatments, *Theor. Appl. Fract. Mec.* 118 (2022) 103214.
- [30] Y. Meng, H. Jing, Z. Zhou, L. Zhang, S. Sun, Experimental investigation on the mixed-mode fracture behavior of rock-like material with bedding plane, *Theor. Appl. Fract. Mec.* 117 (2022) 103159.
- [31] G. Ji, K. Li, G. Zhang, S. Li, L. Zhang, An assessment method for shale fracability based on fractal theory and fracture toughness, *Eng. Fract. Mech.* 211 (2019) 282–290.
- [32] D. Wu, L. Yu, H. Su, S. Geng, T. Zhang, C. Wei, The effects of three-dimensional bedding on shale fracture behavior: Insights from experimental and numerical investigations, *Eng. Fract. Mech.* 307 (2024) 110295.
- [33] M.D. Kuruppu, Y. Obara, M.R. Ayatollahi, K.P. Chong, T. Funatsu, ISRM suggested method for determining the mode I static fracture toughness using semi-circular bend specimen, *Rock Mech. Rock Eng.* 47 (2014) 267–274.
- [34] T. Ai, R. Zhang, H.W. Zhou, J.L. Pei, Box-counting methods to directly estimate the fractal dimension of a rock surface, *Appl. Surf. Sci.* 314 (2014) 610–621.
- [35] Z.H. Zhou, S.J. Du, 3D statistic analysis of geometrical properties of a rock joint, *Rock Soil Mech.* 26 (2005) 1227–1232.
- [36] N. Barton, V. Choubey, The shear strength of rock joints in theory and practice, *Rock Mech.* 10 (1977) 1–54.
- [37] Q. Yin, R. Liu, H. Jing, H. Su, L. Yu, L. He, Experimental Study of Nonlinear Flow Behaviors through Fractured Rock Samples after High-Temperature Exposure, *Rock Mech. Rock Eng.* 52 (2019) 2963–2983.